

# FISSION-RESIDUES PRODUCED IN THE SPALLATION REACTION $^{238}\text{U} + \text{p}$ at 1 A GeV.

M. Bernas<sup>a</sup>, P. Armbruster<sup>b</sup>, J. Benlliure<sup>b,c</sup>, A. Boudard<sup>d</sup>,  
E. Casarejos<sup>c</sup>, S. Czajkowski<sup>e</sup>, T. Enqvist<sup>b 1</sup>, R. Legrain<sup>d†</sup>,  
S. Leray<sup>d</sup>, B. Mustapha<sup>a 2</sup>, P. Napolitani<sup>b,a</sup>, J. Pereira<sup>c</sup>,  
F. Rejmund<sup>b,a</sup>, M.-V. Ricciardi<sup>b</sup>, K.-H. Schmidt<sup>b</sup>,  
C. Stéphan<sup>a</sup>, J. Taieb<sup>b,a 3</sup>, L. Tassan-Got<sup>a</sup>, C. Volant<sup>d</sup>.

<sup>a</sup>*Institut de Physique Nucléaire, 91406 Orsay Cedex, France*

<sup>b</sup>*Gesellschaft für Schwerionenforschung, Planckstr. 1, 64291 Darmstadt, Germany*

<sup>c</sup>*Universidad de Santiago de Compostela, 15706 Santiago de Compostela, Spain*

<sup>d</sup>*DAPNIA/SPhN, CEA/Saclay, 91191 Gif sur Yvette Cedex, France*

<sup>e</sup>*CEN Bordeaux-Gradignan, Le Haut-Vigneau, 33175 Gradignan Cedex, France*

---

## Abstract

Fission fragments from 1 A GeV  $^{238}\text{U}$  projectiles irradiating a hydrogen target were investigated by using the fragment separator FRS for magnetic selection of reaction products including ray-tracing and  $\Delta E$ -ToF techniques. The momentum spectra of identified fragments were analysed to provide isotopic production cross sections, fission-fragment velocities and recoil momenta of the fissioning parent nuclei. Besides their general relevance, these quantities are also demanded for applications. Calculations and simulations with codes commonly used and recently developed or improved are compared to the data.

*Key words:* NUCLEAR REACTION  $\text{p}(^{238}\text{U}, \text{x})$ ,  $E = 1$  GeV/nucleon; Measured primary fission cross sections of 733 isotopes from Ni up to Eu; Measured fission fragment velocities; Inverse-kinematics method; In-flight separation by high resolution magnetic spectrometer; Identification in  $Z$  and  $A$  by ToF and energy-loss measurements; Relevance for accelerator-driven subcritical reactors and for production of radioactive beams.

*PACS:* 24.75.+i; 25.40.Sc; 25.85.Ge; 28.50.Dr; 29.25.Rm

---

<sup>1</sup> Present address: University of Jyväskylä, 40351 Jyväskylä, Finland

<sup>2</sup> Present address: Argonne National Laboratory, Argonne, IL 60439, USA

<sup>3</sup> Present address: CEA/Saclay DM2S/SERMA/LENR, 91191 Gif/Yvette CEDEX, France

## 1 Introduction

Fission of heavy nuclei excited at high collision energies has been investigated for the last decades. Produced by fragmentation or proton collision, the excited nuclei release their energy by emitting neutrons and charged particles, and eventually by fission. At low excitation energy, close to the fission barrier the probability of fission for nuclei around U stays constant or decreases at increasing excitation energy (first chance fission). Increasing further the excitation energy, two opposite tendencies are observed. High excitation energy and emission of charged particles reduce the probability of fission. On the other hand, neutron emission produces more and more fissile nuclei, enhancing fission. For the highest excitation energies, lighter elements which are less fissile, are created and finally fission vanishes. The competition between the various decay channels provides keys to understand the structure of hot nuclei, level densities, dissipation and disappearance of shell effects with excitation energy.

One of the first experimental approaches to the question of competition of the different decay-channels was opened with radiochemical and off-line mass separator techniques. G. Friedlander et al. [1] studied isotopic production of the alkaline elements rubidium and cesium in  $p + U$  and  $p + W$  reactions at various energies. This pioneering work already characterises the evolution of the symmetric breaking of the excited fragmentation residues as a function of the incident energy. A decade later, similar measurements on alkalines were undertaken using on-line mass separators [2,3] which we will use as a basis for comparison in the following. Meanwhile many results evaluated in reference [4] were obtained to complete these first studies.

The energy dependence of the reactions already studied in reference [1] must be known and controlled for all applications. Until now this aspect has been explored by radiochemistry and  $\gamma$ -spectroscopy. The systems  $p + Pb$  [5] and  $p + Bi$  [6] were extensively investigated by using off-line  $\gamma$ -spectrometry in a wide range of energies.

Why do we start new studies on this question ? The new experimental equipment operating at GSI offers an efficient way to separate isotopes in inverse kinematics at relativistic energies. A 1 A GeV U-beam is delivered at the heavy-ion synchrotron (SIS), and in-flight separation techniques become applicable to all the energetic U residues. The inverse kinematics at relativistic energies provides fully ionised forward-focussed fragments which are separated by using the FRagment Separator (FRS) and identified by energy loss ( $\Delta E$ ) and time-of-flight (ToF) measurements. Each of the isotopic cross-sections can

be determined, and the kinematics of every residue can also be reconstructed. Based only on physical properties of the ions, the method does not depend on chemistry. As beta-decay half-lives are much longer than the 0.3  $\mu$ s separation time, primary residues are observed.

One of the important findings of the combination of the relativistic U beam at SIS with the FRS separation techniques was the identification and yield measurement of 117 new neutron-rich nuclei down to the sub-nanobarn level, among which the doubly-magic nucleus  $^{78}\text{Ni}$  [7,8]. The efficiency, selectivity and high sensitivity of the method was clearly demonstrated. It triggered new efforts to produce beams of exotic nuclei by in-flight techniques.

Apart from the scientific interest of proton induced spallation reactions, applications were soon looked upon. For the purpose of Accelerator Driven Systems (ADS), for energy production and transmutation of nuclear waste [9], a great number of data sets were missing. Spallation targets for neutron-sources require extensive data in the same domain. Patents were approved in Germany and France [10]. Thus a campaign of systematic measurements was undertaken to obtain isotopic production cross-sections for a number of systems with an accuracy of about 10% and an improved understanding of reaction mechanisms in order to interpolate to other systems and energies below 1 A GeV.

For this purpose, at 800 A MeV Au + p [11–13], Pb + p at 1 A GeV [14,15] and at 0.5 A GeV, Pb + d at 1 A GeV [16] and spallation from 1 A GeV U + p [17] and 1 A GeV U + d [18] were already studied and published. The missing part is still under analysis. Spallation of Fe on p and d was measured between 0.3 and 1.5 A GeV. Very recently, the systems Xe + p and Xe + d were measured between 0.2 and 1 A GeV to conclude this experimental program.

In this article we report on the (U + p)-fission products measured at 1 A GeV. The system plays the role of a prototype for high-energy nucleon-induced fission of an actinide. At high energies, data on fission of  $^{238}\text{U}$  induced by protons can be used as a benchmark for other actinide nuclei present in incineration situations.

The results on fission-residues in spallation of 1 A GeV  $^{338}\text{U}$  on protons together with our results on evaporation-residues [17] bring a comprehensive overview on this system. Earlier results on U-projectile fission were obtained on Pb [19–22] and on Be [23] targets. Altogether they should lead to a coherent reconstruction of the intermediate systems after the primary cascade and nucleon evaporation preceding fission. The reproduction of the data with standard codes, the intra-nuclear cascade-evaporation model LAHET [24] is far from being satisfactory. Improvements of codes have been published [25–28], and are applied here.

Finally, the new data on isotopic yield measurements for  $^{12}\text{C}$  and  $^{13}\text{C}$  together with present and coming data on their energy dependence should provide a reference in order to control nuclide production in the forthcoming applications of proton-induced spallation.

## 2 Experiment

### 2.1 Experimental set-up

Uranium-ions delivered by the Penning source are accelerated in the UNILAC and post-accelerated in the SIS of GSI-Darmstadt. The beam energy of the  $^{238}\text{U}^{76+}$  ions on target is 1 A GeV and their velocity  $\beta_0 = 0.876$ . The average time structure is a pulse of 7 s every 13 s. The beam intensity delivered is  $10^6$  to  $10^8$  ions/pulse. It is controlled and monitored prior to the target by means of a secondary electron chamber, called SEETRAM [29].

A plastic target could not be chosen, since the production yields from C prevail upon the H yields in the mass region intermediate between fragmentation and fission. The uncertainties in the sharing between C and H in a plastic-target would not be consistent with our accuracy requirements.

The liquid hydrogen target used in the present experiment consist of a  $(1.25 \pm 0.03)$  cm thick circular cell closed by two thin parallel titanium windows. The cell is located at the bottom of an helium cryostat. Surrounding the cell, thin aluminised mylar reflectors and external titanium windows ensure thermal and vacuum insulation [30]. The hydrogen thickness of  $(87.2 \pm 2.2)$  mg/cm<sup>2</sup> [11] is chosen to obtain a 10% reaction probability. The Ti target walls have a total thickness of  $(36.3)$  mg/cm<sup>2</sup>. Their contribution to the counting rates remains below 10%. It has been measured systematically using a “dummy” target of the same composition as the empty target cell.

### 2.2 Separation and identification in A and Z

At energies close to 1 A GeV, fission fragments are observed up to  $Z = 72$  and they are nearly totally stripped. In the worst case at  $Z = 72$ , less than 15% of the ions still carry electrons [31]. They are momentum analysed with the fragment separator FRS, a double-stage achromatic spectrometer with an intermediate dispersive image plane S2 and a final image plane S4 [32]. A schematic view of the FRS and detectors is shown in Fig. 1.

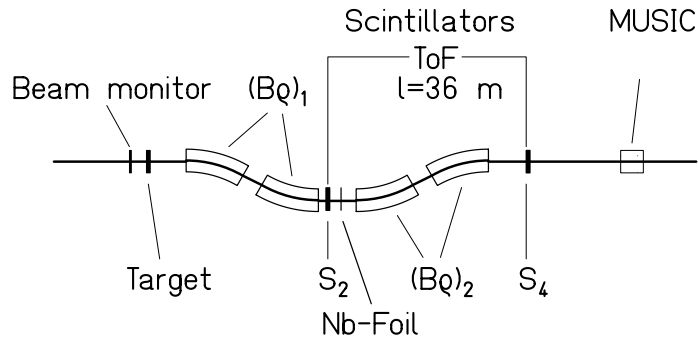


Fig. 1. Schematic view of the fragment separator with the detector equipment.

In S4 the separated fragments are identified in  $Z$  by their energy losses measured in a four-stage ionization chamber, MUSIC [33]. The mass number  $A$  of the analysed fragments is determined from a measurement of velocity and magnetic rigidity between S2 and S4. The measurement is performed by two position sensitive plastic scintillators [34]. The times and positions in S2 and S4 have to be known accurately in order to correlate the time of flight with the precise length of the flight-path. Fission fragments fill the full phase space defined by the acceptance of the FRS. The presence of the 5 mm thick scintillator in S2 slightly alters the achromaticity of the FRS. Nevertheless 36 elements from  $Z = 28$  to 64 are simultaneously transmitted to S4. Signals from the S4 scintillator trigger the data-acquisition system. Mass and charge numbers are calibrated by comparison to the parameters of the primary uranium beam and by using the known structure of fission yields in the asymmetric fission domain.

### 2.3 Constitution of the momentum spectra

The momentum acceptance of the FRS is 3 %. Applying the basic relation

$$B\rho = \frac{\beta\gamma \cdot A}{Z} \times \frac{c \cdot m_0}{e} \quad (1)$$

with  $Z$  and  $A$  numbers determined, a 3 % fraction of the  $\beta\gamma$  spectrum is obtained for each measurement. The total spectrum of transmitted fission fragments covers a range of 7 % to 20% of the reduced momentum of the projectile,  $\beta_0\gamma_0$ . The measurements consist of a 2 % step-by-step scanning of the FRS magnetic fields tuned on cadmium, ( $Z = 48$ ). After normalisation to the incoming dose given by the SEETRAM, and dead-time corrections, complete  $\beta\gamma$  distributions are reconstructed by assembling about 10 files of overlapping  $B\rho$  settings to produce a  $\beta\gamma$  spectrum for each of the isotopes;

$$\frac{dn(\beta\gamma)}{d(\beta\gamma)} = \frac{n_i(\beta\gamma)}{N_i(1 - T_i)} \quad (2)$$

where  $n_i(\beta\gamma)$  is the  $i^{\text{th}}$  bin of the  $\beta\gamma$  spectrum,  $T_i$  is the dead time fraction and  $N_i$  the number of incident ions for this measurement. All in all  $4 \cdot 10^6$  events were accumulated.

Fragments are spread over 20 cm in the image plane at S2 covered by the first position-sensitive scintillator. For an identified isotope the distribution in S2 depends only upon  $\beta\gamma$ , and the accuracy on S2 position governs the accuracy of the magnetic rigidity. In the present case, a precision in position of 2.5 mm (FWHM) leads to a resolving power of  $\beta\gamma / \Delta\beta\gamma = 2600$ , given the dispersion in momentum of the first stage of the FRS by percent,  $D = 6.5 \text{ cm}/\%$ . In this experiment the response of the scintillator was slightly non-linear, and a routine was systematically used in the analysis software to correct for this, [11].

The FRS magnetic fields tuned on  $Z = 48$  guide this element to the center of S4 and display on both sides the neighbouring elements, gradually apart from the center of S4. The 36 elements are transmitted together to the final focus S4, and momentum distributions of the produced isotopes are simultaneously measured in one series of  $B\rho$  settings of the FRS. The  $\beta\gamma$  spectra can be converted to the projectile frame and are presented in cm/ns as velocity spectra in the system of the projectile. This coordinate system is appropriate for comparison with previous results concerning fission from target nuclei. Moreover, at high excitation energy, fission fragments are emitted isotropically in the fissioning system [19,35]. This allows for analytical formulations to be used in the analysis of the  $\beta\gamma$  distributions.

#### 2.4 Description of the velocity spectra

The reconstructed velocity spectra are the corner stones of our analysis. An example of the velocity spectrum is shown in Fig. 2b. Two narrow asymmetric peaks are observed roughly equidistant from velocity zero, i. e. the projectile velocity. Velocities are defined in reference to the beam direction i. e. forwardly and backwardly emitted fragments have positive and negative velocities, respectively. The velocities of the fission fragments arise from their Coulomb repulsion at scission. Velocity vectors of a specific isotope populate a thin spherical shell in the fissioning system, which may be slightly shifted compared to the projectile system by the primary reaction recoil. The sphere is pictured in Fig. 2a by a circle, the cut of the sphere by a plane which contains the beam. Only forward and backward cups of the sphere, defined by the angular acceptance of the FRS  $\alpha$ , are transmitted, and the longitudinal projections of their velocity distributions are shaping the two peaks (Fig. 2b).

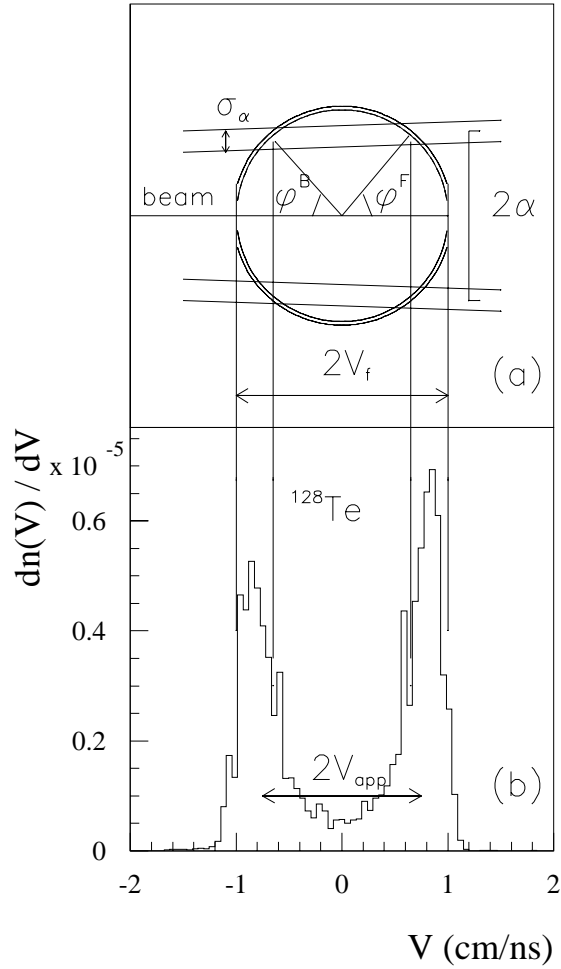


Fig. 2. a) Schematic view of the experimental parameters shaping the measured velocity spectrum in the frame of the fissioning system.  $V_f$  is the fission-fragment velocity,  $\alpha$  is the angular acceptance of the FRS, and  $\sigma_\alpha$  its variance.  $\varphi^{B,F}$  are the corresponding emission angles of fission fragments in the fissioning system in forward and backward directions, respectively. b) Velocity spectrum of  $^{128}\text{Te}$  in the frame of the fissioning system. The velocity  $V = 0$  refers to the projectile frame.  $V_{app}$  is the apparent fission velocity defined in the text.

For selected elements the velocity spectra of all isotopes are presented on scatter-plots in Fig. 3. Rates are given in terms of velocities and of neutron number  $N$ . They all show strongly populated areas along two parallel lines associated to backward and forward emitted fission fragments. The lines, almost symmetric in respect to the axis ( $V = 0$ , i.e. projectile frame), show a fission fragment velocity decreasing with increasing atomic number  $Z$  of

the fragment, a trend due to momentum conservation in fission. The parallel lines contrast with U + Pb scatter-plots [22] where 1) neutron-rich nuclei are strongly enhanced for zirconium and tellurium due to electromagnetic fission and 2) fragmentation residues sit in between the forward and backward regions for neutron-deficient isotopes. In spite of the absence of evaporation residues, at decreasing masses of the lighter elements, events with small velocities are found. Besides the small contribution of fragmentation residues produced in target windows, this is a first indication for the contribution of secondary reactions which will be discussed in the following section.

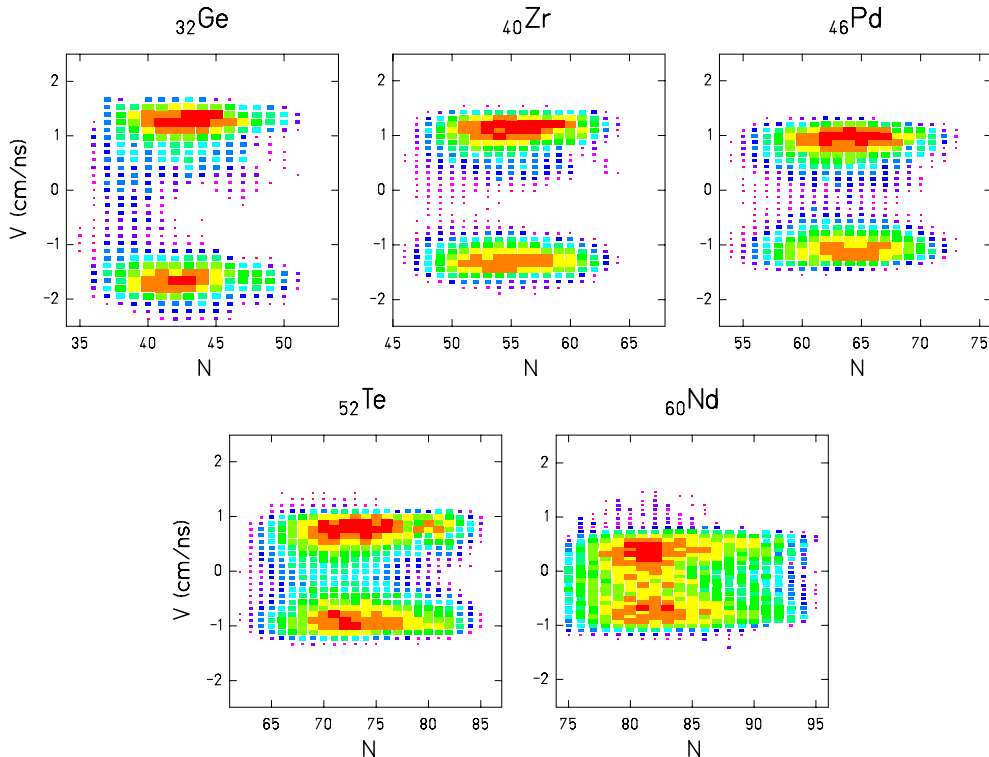


Fig. 3. Cluster plots of number of events measured on target in terms of velocity versus neutron number. The fission velocity coordinate is given in the center of mass of the projectile. The intensity scale is logarithmic with a factor of 2 between adjacent colours.

Data taken on the “dummy” target show the same pattern as in Fig. 3 with a contribution of fragmentation. Yields are defined by the integrated velocity spectra. Isotopic distributions of yields in the ”dummy” and in the target are compared in Fig. 4. As intended, the yields in the “dummy” are only a few % of the yields in the target, except in the neutron-deficient region where they reach larger values, but less than 20% . Asymmetric fission, leading to neutron rich isotopes, is also clearly enhanced for titanium relatively to hydrogen. The hydrogen contribution is obtained by subtracting the yields on the ”dummy” from the target yields. Uncertainties are estimated from the fluctuations of



the intensity ratio of the two peaks, as will be discussed later. The error bars on yields measured for the “dummy” are negligible when reported to yields on hydrogen.

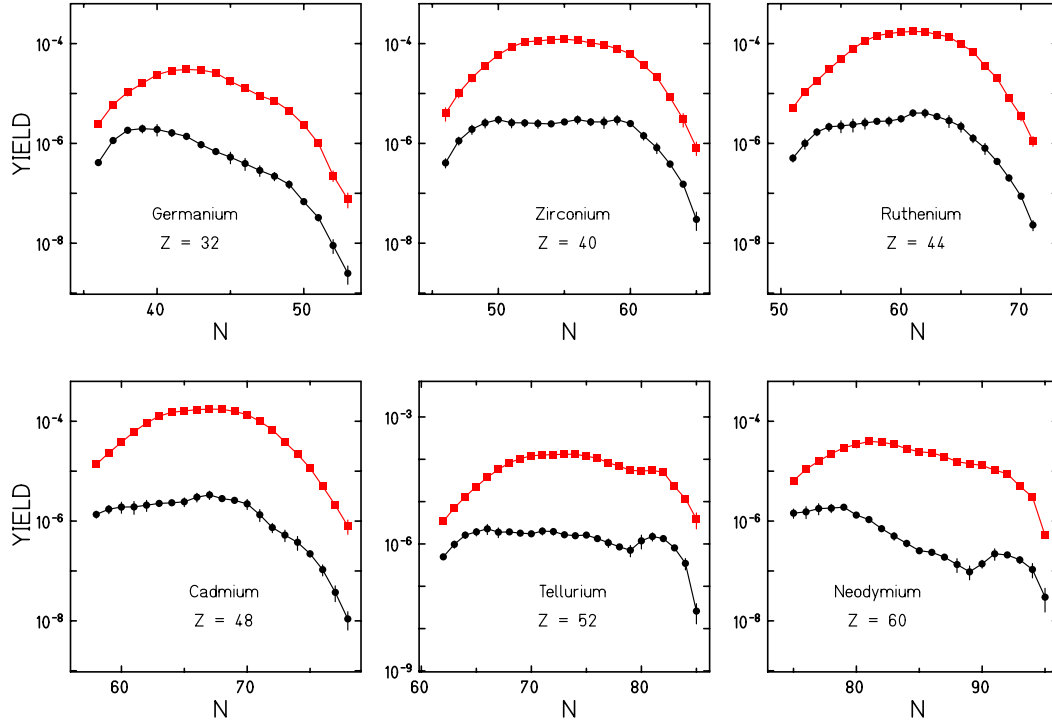


Fig. 4. Comparison of transmitted yields [arb. units] of isotopes on hydrogen (squares) and “dummy” (circles) targets as a function of their neutron number for selected elements.

Evaluating velocities, the  $\beta\gamma$  distributions on target and “dummy” are found to be very similar for a given isotope, and the yield of the “dummy” is on a few percent level. Therefore, the contribution of the titanium windows could be ignored in the evaluation of fission-fragment velocities in  $U + p$ .

### 2.5 Fission velocity and transmission

The geometrical aperture of the spectrometer seen from the target defines a solid angle  $\Omega$  simply related to the angular acceptance  $\alpha$  assuming axial symmetry.  $\alpha$  is the limiting value for the emission angle  $\phi$  of transmitted fission fragments in the laboratory system.  $\phi$  corresponds to angles  $\varphi^F$  and  $\varphi^B$  in the fissioning system with F and B set for forward and backward, respectively, see Fig. 2a. The angular transmission  $T_\Omega$  is defined as the ratio of the yield measured for a given fission fragment to the total production yield for this fragment.

The determination of  $T_\Omega$  is a key to obtain the cross-sections. It depends upon fission fragment velocities and it must be evaluated for each fragment.

$T_\Omega$  is a function of the three variables  $\alpha$ ,  $\beta_0$  representing the beam and  $\beta_f$  the fission process with  $V_f = \beta_f c$ , the fission velocity, i.e. the radius of the sphere shown in Fig. 2a. As shown in Appendix 1, for a bundle of particles with an angular divergence  $\alpha$  starting from a point-like source and entering the FRS on its principal trajectory, the transmission  $T_\Omega$  can be calculated rigorously, without any approximation, when setting the variances to zero. In the fissioning system,  $T_\Omega$  is obtained by integrating the surface elements of the spherical velocity shell within the two solid angles, and we obtain [22]:

$$T_\Omega = T_\Omega^B + T_\Omega^F = 1 - \frac{\cos \varphi^F + \cos \varphi^B}{2} \quad (3)$$

In Fig. 2b the velocity distribution of transmitted  $^{128}\text{Te}$  is given as an example. Three quantities are evaluated from these distributions:

- 1) The spectrum  $dn(\beta\gamma) / d(\beta\gamma)$  integrated over the whole range of  $\beta\gamma$ , evaluated for each of the isotopes gives the measured yields.
- 2) A shift of the mean velocity of forward and backward emitted fission fragments, compared to the projectile velocity ( $V = 0$ ) gives the velocity of the fissioning parent nucleus, the recoil velocity.
- 3) The centroid of each of the two peaks defines a mean fission-fragment velocity, the apparent velocity  $\beta_{app}^{F,B} = V_{app}/c$  different for forward and backward emitted fragments. We define the mean value of the two apparent velocities,

$$\beta_{app} = \frac{|\beta_{app}^F| + |\beta_{app}^B|}{2} \quad (4)$$

The two peaks are shaped by the variances of the three variables  $\alpha$ ,  $\beta_0$  and  $\beta_f$ , as will be shown later by a Monte-Carlo simulation. With all variances set to zero -Fig. 5a- the peaks become rectangles, as the phase-space density of a spherical homogeneously filled shell per interval  $d\beta_{||}$  with  $\beta_{||}$  the longitudinal velocity, is constant. The projection of the spherical shell on the beam axis is a rectangle. In this case the apparent velocity of forward and backward emitted fission fragments (see Fig. 2) is given by:

$$\beta_{app}^{F,B} = \beta_f - \frac{\beta_f - \beta_f \cos \varphi^{F,B}}{2} = \beta_f \frac{1 + \cos \varphi^{F,B}}{2}$$

and the mean value follows:

$$\beta_{app} = \frac{\beta_f}{2} \left( 1 + \frac{\cos \varphi^F + \cos \varphi^B}{2} \right) \quad (5)$$

with eq. (5) defining the transmission, we obtain the fission velocity depending on  $\beta_{app}$  and  $T_\Omega$ :

$$\beta_f = \frac{2\beta_{app}}{2 - T_\Omega} \quad (6)$$

from which the limiting cases are deduced  $\beta_f = \beta_{app}$  for  $T_\Omega = 0$ , and  $\beta_f = 2\beta_{app}$  for  $T_\Omega = 1$ .

In Appendix 1 we show that with  $\varphi_\Sigma = (\varphi^F + \varphi^B)/2$  the fission fragment velocity  $\beta_f$  and the transmission  $T_\Omega$  are given in very good approximation by:

$$\beta_f = \beta_{app}[1 + (\tan \varphi_\Sigma/2)^2] \quad (7)$$

$$T_\Omega = \frac{2}{1 + [\cot \varphi_\Sigma/2]^2} \quad (8)$$

with

$$\tan(\varphi_\Sigma/2) = \frac{\beta_{lim}}{2\beta_{app}} \quad (9)$$

$\beta_{lim}$  is defined by  $\alpha$  and the velocity of the fissioning parent nucleus  $\beta$  approximated by  $\beta_0$

$$\beta_{lim} = \alpha\sqrt{\gamma^2 - 1} \approx \alpha\beta_0\gamma_0 \quad (10)$$

Eq.(7) and (8) demonstrate the central importance of the ratio  $\beta_{lim}/2\beta_{app}$ .

Summarising the procedure:

- From the  $\beta\gamma$  distribution, the mean apparent velocity  $\beta_{app} = (\beta_{app}^F + \beta_{app}^B)/2$  is evaluated for each isotope.
- $T_\Omega$  and  $\beta_f$  are simple functions of the mean opening angle  $\varphi_\Sigma = (\varphi^F + \varphi^B)/2$ .
- $\beta_{lim}$  is related to the acceptance angle  $\alpha$  of the spectrometer and to the projectile velocity  $\beta_0$

In order to include the variances on the FRS angular acceptance and the kinematics of fissioning nuclei, we have simulated the physical cut in phase space due to the angular acceptance of the FRS. The purpose is to relate  $V_f$  and the transmission to the measured  $V_{app}$ .

The Monte-Carlo calculation is based on the following assumptions:

- 1) In the system of the fissioning parent nucleus, approximated by the system of the projectile nucleus, fission fragments are isotropically emitted with a given velocity  $V_f$ .
- 2) The spherical shell of velocity vectors is converted to the laboratory system moving relativistically with a velocity  $\beta$ . Fragments emitted within the FRS acceptance angle  $\alpha$  are transmitted. At this stage we obtain a transmission value and the momentum spectrum in the laboratory system.
- 3) This spectrum is reconverted into the projectile system.
- 4) Variances of velocities and of the acceptance angle are further parameters which are included.

The simulation enlightens the effects of the experimental constraints on the measurement. On Fig. 5a the forward and backward rectangles correspond to the share of transmitted fission-fragments with  $\sigma_\alpha = 0$ . A filled rectangle would be obtained for  $\beta_f$  smaller than  $\alpha\beta\gamma$  and  $T_\Omega$  would then reach 100 %. The second curve in the same frame results from the introduction of a variance of the acceptance angle  $\sigma_\alpha = 2.5$  mr derived from the known geometry of the FRS [36,37]. It shows that the filling of the spectra at intermediate velocities comes mainly from the large variance of the FRS acceptance angle.

Fig. 2b versus Fig. 2a shows that the external slopes depend only on the fluctuations of the reduced momenta of the fission fragments and/or of the fissioning nuclei. Several sources contribute to these fluctuations - fission fragment velocities, target location straggling and recoil momenta of the fissioning nuclei -, and lead to a broadening of the peaks as illustrated on Fig. 5b. The relative contributions of these sources are quantified in the discussion, see sect. 4.8.

With  $\sigma_{\beta\gamma} = 7.10^{-3}$  the external slopes are almost vertical and the value of  $V_f = 1.2$  cm/ns introduced in the simulation can be extracted from the distance between the external sides at half maximum. On the contrary, if  $\sigma_{\beta\gamma}$  becomes larger than the width of the rectangles of Fig. 5a, this half-maximum rule is no longer valid, as seen for  $\sigma_{\beta\gamma} = 14.10^{-3}$ . A value of  $\sigma_{\beta\gamma} = 7.10^{-3}$  is selected as an “empirical broadening” to optimize the simulation. The result is illustrated in both examples of Fig. 6a and 6b.

The relation between  $V_{app}$  and  $V_f$  either from eq. 6 or from the simulation are very close as shown in Fig 7(a) and the trends at  $T_\Omega = 0$  or 1 are correct

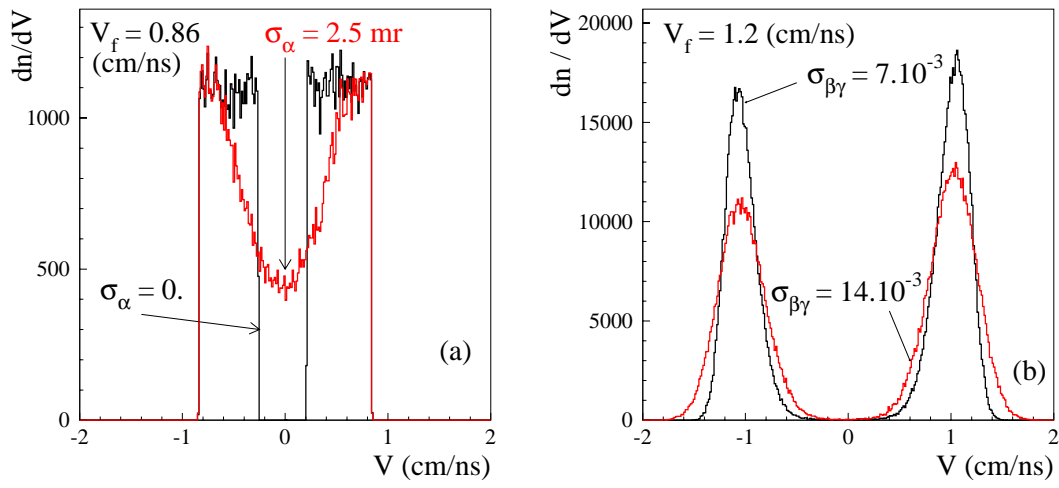


Fig. 5. Impact of variances a)  $\sigma_\alpha$  of  $\alpha$ , the acceptance angle of the FRS, and b)  $\sigma_{\beta\gamma}$  of  $\beta\gamma$ , the momentum of the fissioning nucleus. Fission-velocities are different in a) and b) in order to better illustrate the contributions of both variances.

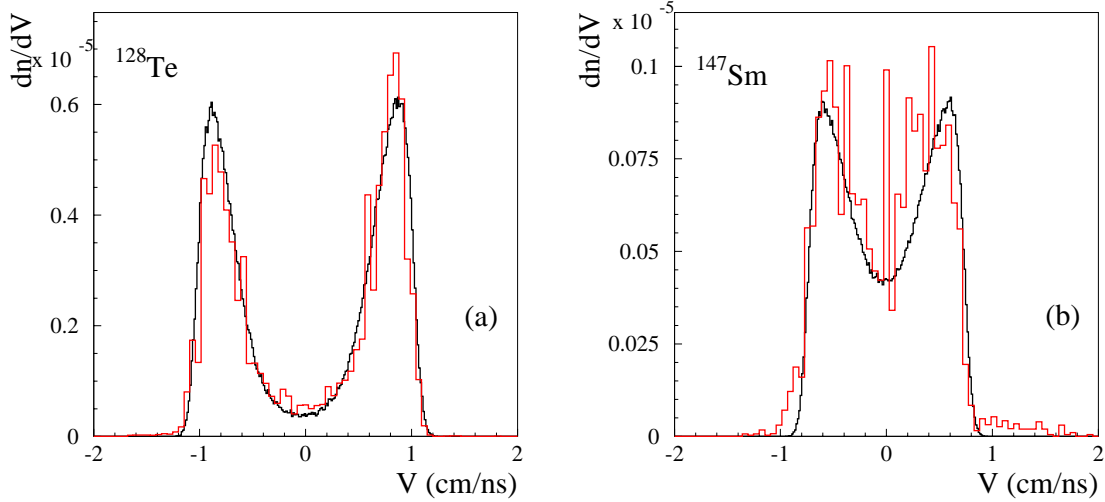


Fig. 6. Examples of simulation with  $\sigma_\alpha = 2.5$  mr  $\sigma_{\beta\gamma} = 7.10^{-3}$  compared with the measured spectra for  $^{128}\text{Te}$  and  $^{147}\text{Sm}$ .

in both cases. Simulated and calculated values of  $T_\Omega$  are the same for fission velocities larger than 0.8 cm/ns ( Fig. 7b). For smaller velocities the calculations, which do not include the large variance of the acceptance angle, cannot describe the transmission. Approaching  $T_\Omega = 1$  the simulation accounting for the variances provides better results. It is seen on the velocity spectra of isotopes of neodymium to gadolinium where a few isotopes (the heaviest isotopes

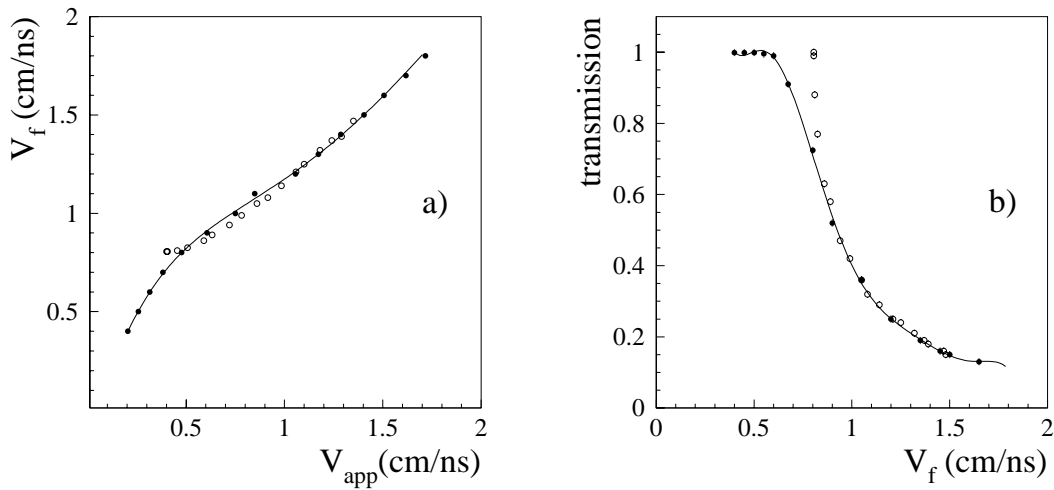


Fig. 7. Fission fragment velocity as a function of apparent velocity a) and transmission b) as a function of fission fragment velocity given by the simulation (full points) and calculations (empty points) using eqs. (7) and (8). Lines are fits to the full points.

showing the largest fission velocities) still show a residual valley between forward and backward peaks. In the following transmissions and fission fragment velocities are obtained using the values of  $V_{app}$  determined for each isotope and the fitted curves of Fig. 7.

### 3 Experimental results

#### 3.1 Fission fragment velocities

The velocity spectrum of each isotope has been analysed to extract a value of the apparent velocity. The apparent velocities have been converted into fission fragment velocities. For a given element, the fission fragment velocity decreases smoothly from a maximum value for the heaviest isotopes down to values smaller by 10% for the lighter isotopes, Fig. 8. Further down to the most neutron-deficient isotopes, the velocities fall abruptly. In case of U+p, this fall cannot be related to the occurrence of evaporation residues since this process does not populate the neutron-deficient region of fission fragments. The small contribution from fragmentation yields in the Ti-windows (Fig. 4) cannot explain the observed fall in velocity of 20%. This fall is due to secondary reactions in which heavier primary fission fragments loose nucleons in a secondary fragmentation reaction in the target. Atomic numbers and masses are reduced, whereas the velocity spectra are only blurred. These contributions - due to

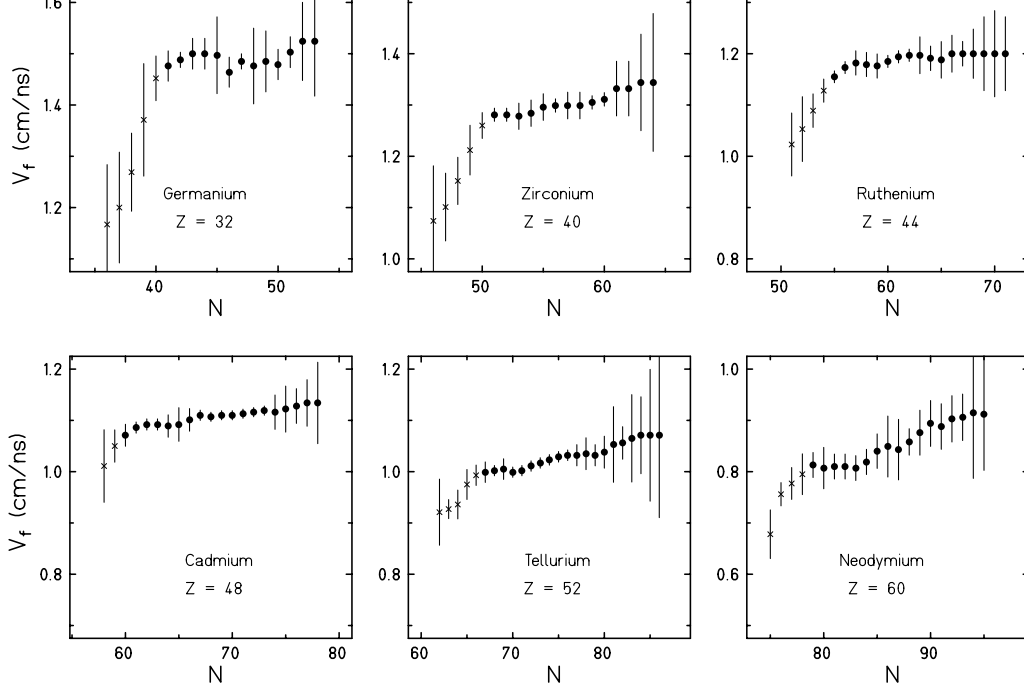


Fig. 8. Fission velocities for selected elements. Cross symbols correspond to regions where secondary-reaction products are mixed with direct fission fragments.

larger  $Z$  with smaller fission-fragment velocities - are superimposed with the spectrum of the primary isotope. This contamination reduces the apparent velocity of the isotope. It becomes significant in the neutron-deficient region where productions by direct fission is low and secondary-reaction products are abundant. However, the small velocities of the lightest isotopes of neodymium cannot be explained by this argument, as secondary reactions of fission fragments contribute little. Here secondary reactions of spallation products could pollute the yields of neutron-deficient fission fragments.

The velocity of an element is taken as the mean value of the velocities for the four isotopes most abundantly populated, in order to select the dominant symmetric fission regime. This velocity is plotted as a function of  $Z$  in Fig. 9a. The uncertainties are less than 4%. Three lines are indicated showing the velocity dependence expected for three values of the nuclear charge of the fissioning parent nucleus  $Z_0 = 92, 86$  and  $80$  [38,39]. The scission configuration of the fissioning nuclei is approximated by the outline of two deformed nuclei ( $\beta_1 = \beta_2 = 0.65$ ) at a given distance. Using momentum conservation, the fragment velocities are calculated for the total kinetic energies released from the scission configuration.

None of the three lines coincides exactly with the data. Fissioning nuclei with  $Z_0$  between 84 and 90 can contribute to the production of fission fragments. The general trend towards smaller fission fragment velocities going from neutron-rich isotopes to neutron-deficient isotopes is observed for all el-

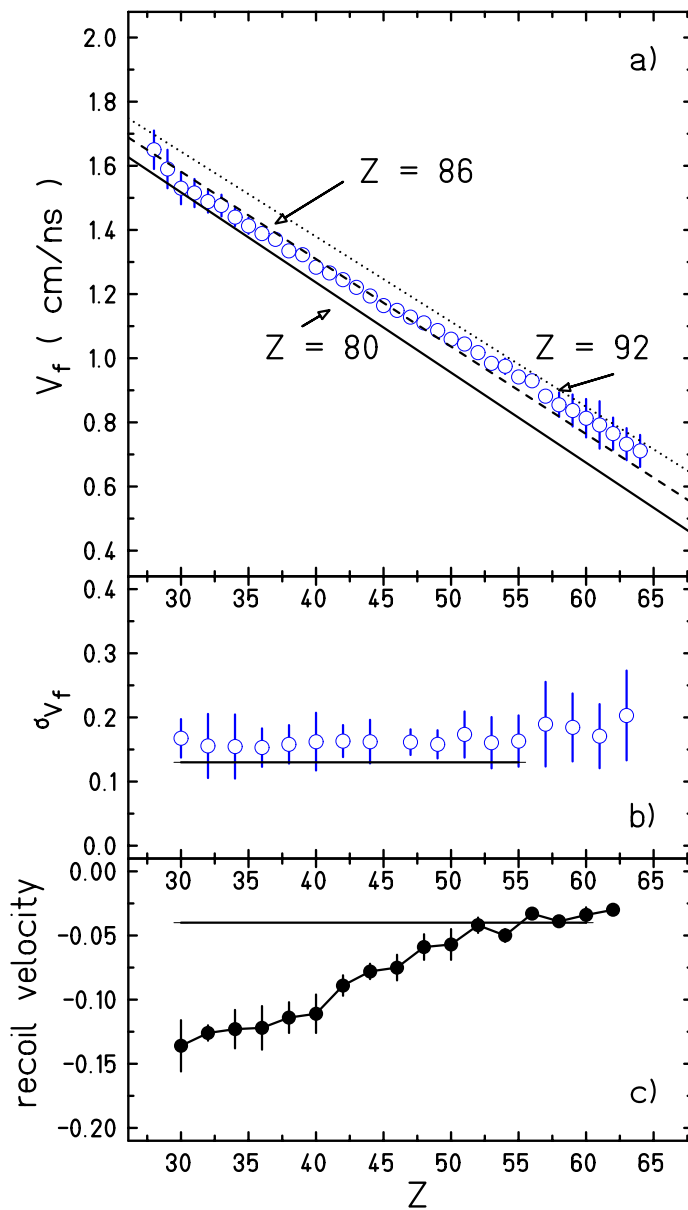


Fig. 9. Fission fragment velocities as a function of  $Z$ . a) The lines are obtained using the calculation of velocity for fissioning parent nuclei of  $Z_0 = 80$  (full line),  $Z_0 = 86$  (dashed line) and  $Z_0 = 92$  (dotted line) with the parametrisation of [38] [39] and a deformation of  $\beta = 0.65$  for both fragments. b) Measured variances of the fission velocities in cm/ns. c) Measured displacement of the mean velocity of forward and backward emitted fragments. The lines indicate the effective broadening b) and the recoil velocity c) as measured for the mean parent-fissioning nucleus [17]- see text sect. 4.8 -.

ements (Fig. 8) corroborating that heavy ( $Z = 90$ ) and light ( $Z = 84$ ) parent nuclei do contribute. The first ones contribute to the more neutron-rich and the last to less neutron-rich isotopes.



The slope of the external edges of the velocity distributions introduced empirically in the simulation (Fig. 5b) as a variance  $\sigma_{\beta\gamma}$  are now evaluated systematically as a function of  $Z$  and plotted in fig. 9b). Unfolding these measured values and the underlying rectangle of the transmitted momenta, fig. 5a, the effective broadening  $\sigma_{V_f}$  is obtained, and given by the line in fig. 9b. Both variances are related by  $\sigma_{V_f} = \frac{1}{\gamma} \cdot \sigma_{\beta\gamma} \cdot c$ . Within the limit of our accuracy this width does not depend on the atomic number. Its mean value is  $\sigma_{V_f} = 0.13$  cm/ns, which corresponds to  $\sigma_{\beta\gamma} \approx 8 \cdot 10^{-3}$  in good agreement with the value of  $7 \cdot 10^{-3}$  empirically deduced in sect. 2.6, from the simulations of the measured spectra (Fig. 5b).

The recoil of the fissioning nucleus is determined from the mean value of the forward and backward fission velocities. The values plotted in Fig. 9c are averaged over the four most abundant isotopes of an element. This recoil is small and it decreases from -0.03 at  $Z = 62$  to -0.13 cm/ns for  $Z = 30$ . We obtain a mean value of -0.08 cm/ns.

### 3.2 From yields to cross sections

Isotopic cross sections of (U + p)-fission are obtained by dividing the production yields on hydrogen by the proper transmission, as presented in sections (2.5) and (2.6). Our final values are compared to those used in the analysis of the parallel experiment U + d at 1 A GeV evaluated by J. Pereira applying a different method [36]. A good agreement is found between both sets of transmission-values evaluated in terms of the fission-fragment velocities.

The correction for secondary reactions occurring in the target has to be applied. All fission fragments, neutron-rich more than proton-rich undergo secondary spallation and the yield is depleted. For neutron-deficient isotopes, the fission yields are increased by secondary evaporation residues. The correction for secondary reactions enhances the share of neutron rich isotopes and reduces neutron-deficient ones. This is the reason for the “hook” shape of this correction already presented in a previous article [15] and calculated more precisely in a forthcoming paper [41]. When they exceed 50 %, cross sections for corresponding isotopes are no longer considered. Our experimental method to determine cross sections of primary residues reaches its limit.

Moreover, small secondary effects need to be corrected for: For fragments not centered in S4, i. e. apart from the optical axis, the FRS acceptance angle and consequently the transmission are slightly reduced. The FRS angular acceptance falls from 14.8 mr on the optical axis down to 13.3 mr at 8 cm apart from the axis in S4 [36]. A smooth parabolic function was used to account for this relative loss in transmission. The correction given in table 1, reaches 14% for elements like nickel and samarium.

Z	S4- shift	sec. react. in SC2	Z	S4- shift	sec. react. in SC2	Z	S4- shift	sec. react. in SC2	atomic charge exchange
28	1.14	1.108	40	1.01	1.13	52	1.02	1.149	1.01
29	1.12	1.11	41	1.005	1.131	53	1.03	1.151	1.01
30	1.105	1.112	42	1.	1.133	54	1.035	1.152	1.01
31	1.09	1.114	43	1.	1.135	55	1.045	1.154	1.015
32	1.08	1.116	44	1.	1.136	56	1.055	1.156	1.02
33	1.065	1.118	45	1.	1.138	57	1.065	1.157	1.028
34	1.055	1.118	46	1.	1.140	58	1.08	1.158	1.034
35	1.045	1.122	47	1.	1.141	59	1.09	1.162	1.04
36	1.035	1.123	48	1.	1.143	60	1.105	1.164	1.05
37	1.03	1.125	49	1.005	1.144	61	1.12	1.164	1.06
38	1.02	1.126	50	1.01	1.146	62	1.14	1.166	1.07
39	1.015	1.128	51	1.015	1.148	63	1.16	1.167	1.08

Table 1

Correction factors applied to the measured yields to account for losses due to 1) the shift in S4 position compared to the central position, 2) the secondary reactions in the SC2-scintillator at S2, and 3) the atomic charge exchange in target and S2-scintillator for  $Z \geq 52$ .

Fragments reacting in the scintillator SC2 at S2 escape the magnetic filter of the second half of the FRS. The related loss increases linearly from 11 % for nickel up to 17 % for gadolinium. It is calculated using the total reaction cross section formulation of Karol [42]. The results are given in table 1 for the range of elements investigated.

A loss by ionic charge exchange occurs, either in the target or in the plastic scintillator S2. Eventhough the probability is small for fission fragments at relativistic energies, this factor, negligible up to tellurium, reaches 9 % for gadolinium. Values, calculated using the code GLOBAL [31] are to be considered for heavy elements as shown in table 1.

### 3.3 Discussion of uncertainties

#### a) Systematic uncertainties

- The uncertainty on the SEETRAM calibration is evaluated to 7 % [29]
- The uncertainty on the transmission is evaluated to 5 %. It is mainly due to the 4 % uncertainty on the fission-fragment velocity.
- The uncertainty on the target thickness was established in a dedicated experiment to 2.5 % [11] for a beam hitting the target in its center. However, an uncertainty of 6 mm in the vertical position of the cryostat supporting the H<sub>2</sub> cell leads to an increased uncertainty of 4 % on the target thickness [17].

- The loss factors given in table 1 are determined with an overall uncertainty of 3 %.

All contributions quadratically added up lead to a total systematic uncertainty of 10 %. This systematic uncertainty is not included in the error bars of the cross sections presented in tables of Appendix 2 and in figures 10-12.

b) Statistical uncertainties

- The single-event uncertainty on the angular transmission is large and mainly determined by the large variance of  $\alpha$ .  $\sigma_\alpha$  is evaluated to 17 % [36]. In comparison the uncertainty on  $\beta_{app}$  is negligible. Taking 50 observed events corresponding to the smallest cross section ( $20\mu\text{b}$ ) as the worst case, the statistical uncertainty for the transmission reaches 4 %. Statistical uncertainties are smaller than the systematic uncertainty.
- Uncertainties for the yields have been determined from the ratio of the rates integrated for forward and backward emitted fragments. The difference between the measured ratio and the kinematically expected ratio, is taken as twice the relative uncertainty of the yields. The absolute uncertainties are given in Fig. 4, Fig. 10-12 and in Appendix 2. For the most abundant isotopes the relative uncertainty is approximately 2 %, that is much less than the systematic uncertainty. For the less abundant isotopes, the statistical uncertainties are dominant and overcome the total systematic uncertainty.

Isotopic cross sections are given in Appendix 2 and their distributions for each of the elements appear in Fig. 10-12. They show a rather regular bell shape with some enhancement in the region of neutron-rich isotopes for elements known as asymmetric fission products. At the maximum of the elemental distributions, cross sections vary from 0.5 mb to 20 mb. Values down to  $20\mu\text{b}$  are measured, mostly in the neutron-rich region not polluted by secondary reactions. On the neutron-deficient side, high rates of secondary reactions limit cross-section measurements to values larger than a few mb.

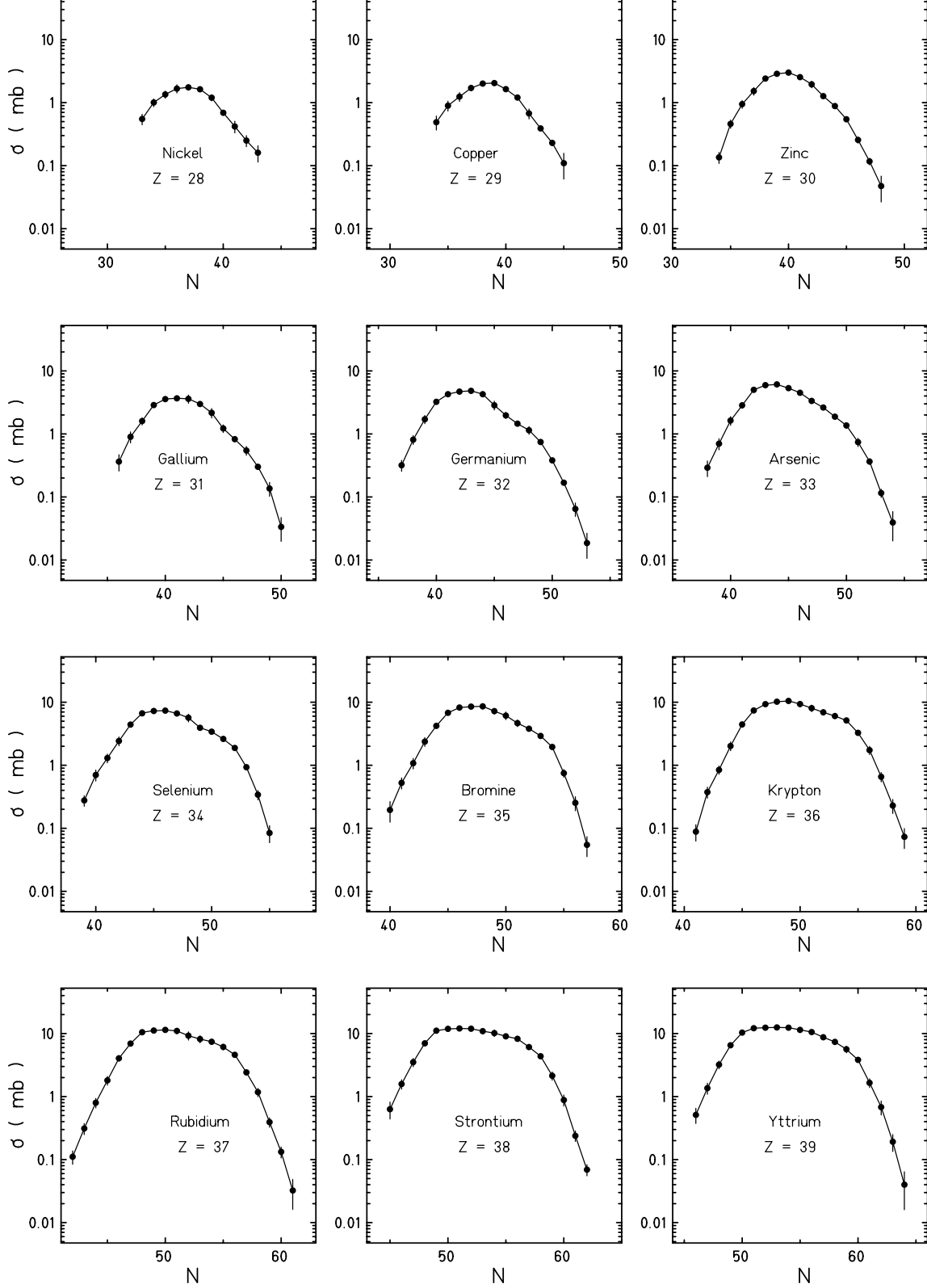


Fig. 10. Isotopic cross sections for fission-fragments in the reaction  $^{238}\text{U}$  1 A GeV + p for elements between  $_{28}\text{Ni}$  and  $_{39}\text{Y}$ .

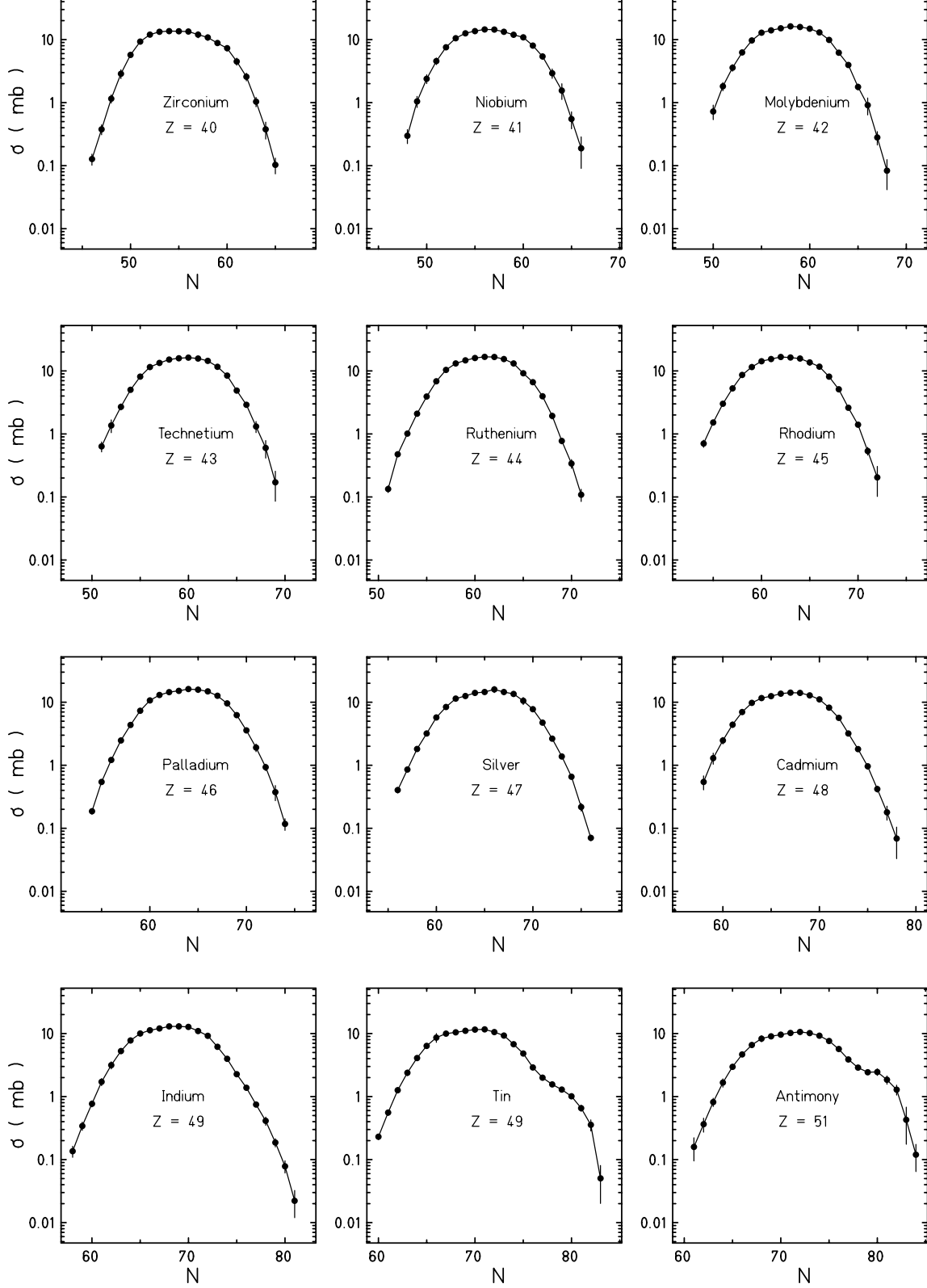


Fig. 11. Isotopic cross sections for fission-fragments in the reaction  $^{238}\text{U} + \text{p}$  at 1 A GeV for elements between  $^{40}\text{Zr}$  and  $^{51}\text{Sb}$ .

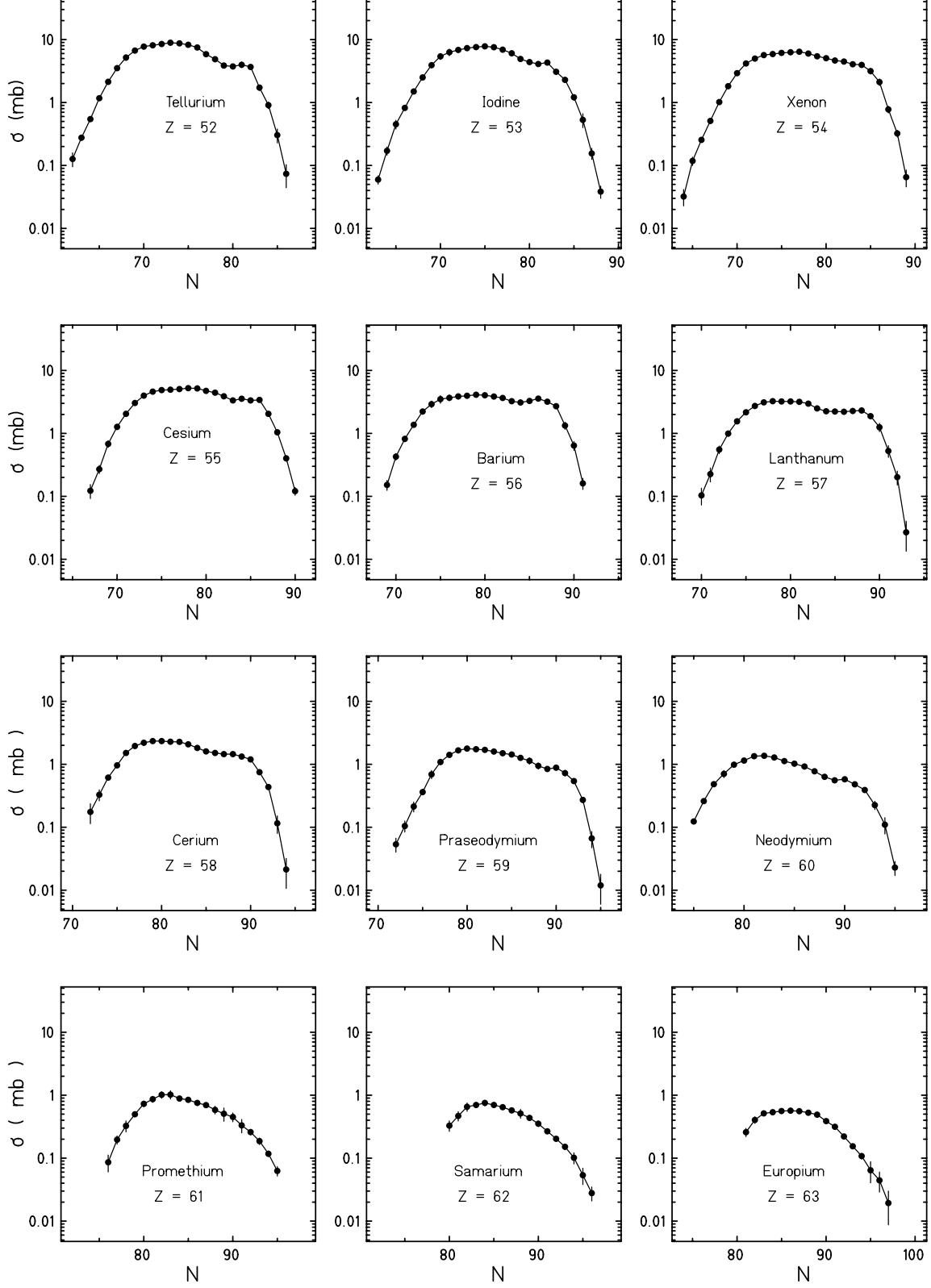


Fig. 12. Isotopic cross sections for fission-fragments in the reaction  $^{238}\text{U}$  1 A GeV + p for elements between  $_{52}\text{Te}$  and  $_{63}\text{Eu}$ .

Measurements of primary isotopic cross sections had been performed for alkalis only. Using fast on-line separator techniques combined with the chemical selectivity of surface ionisation ion-sources [2,3] relative cross sections were obtained covering a wide range of isotopes. The normalisation of the yields to cross sections was based on the results of G. Friedlander [1]. Production yields on U-fission were measured at a proton energy of 24 GeV for isotopes of the complementary elements rubidium and cesium [43]. The distributions are compared to our results in Fig. 13. At 24 GeV, besides fission, evaporation residues populate all elements down to the region covered by fission. Moreover, the excitation energy range covers a wider domain, and evaporation of charged particles and neutrons leads to more neutron-deficient isotopes. The elemental cross sections for both rubidium and cesium are about 75 % of the values presently measured at 1 GeV, in the same ratio as total fission cross sections [4]. In the region of the 8 most neutron-rich fragments, isotopic cross sections are the same as the ones presently measured. The probability to excite the U nucleus with a small excitation energy to produce neutron-rich fragments is independent of the proton energy, as indeed mentioned already in [1].

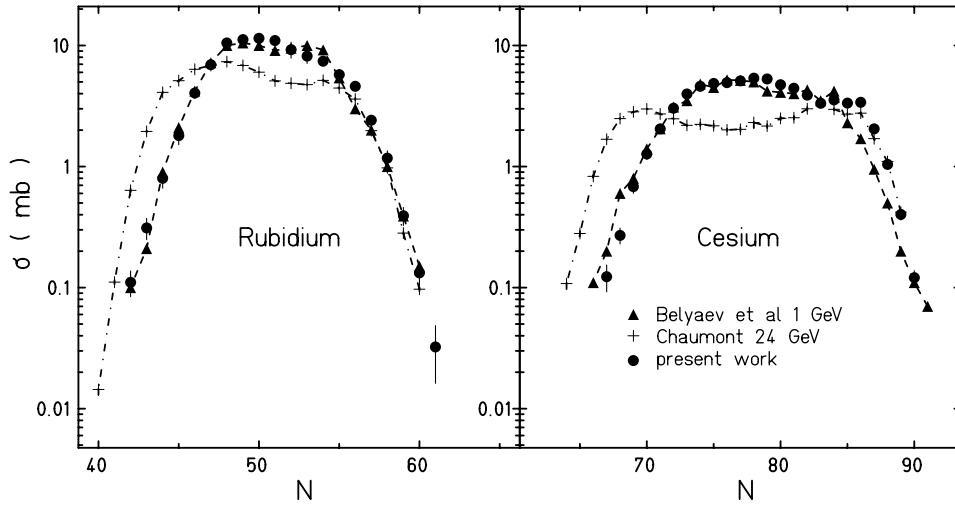


Fig. 13. Comparison of isotopic distributions previously measured by J. Chaumont [43] -dotted-dashed line- and by B. Belyaev [3] -dashed line-with the present data -full points-.

Later the production of the isotopes of cesium and rubidium was investigated for the system  $^{238}\text{U} + \text{p}$  at 1 GeV by using also on-line mass separator techniques [3]. For rubidium our data are very consistent, but cross sections are found larger by a factor 1.8 for the six cesium-isotopes with  $N \geq 85$ , as seen in Fig. 13. In the present experiment, isotopic yields are measured simultaneously for the 36 elements populated in fission, insuring a coherent mass calibration for cesium as for all other elements including rubidium. Moreover the extraction of the asymmetric fission component of all elements achieved

in sec. 4-5 confirms the present mass calibration. Finally the agreement of our isotopic distributions with those of the light elements analysed in the work of [44], also validates our results for the cesium isotopic distribution. In the on-line mass-separator measurement [3] the separation efficiency might have overestimated for these isotopes.

## 4 Features of fission

### 4.1 Elemental cross sections

The elemental cross sections, integrated over isotopes for each element are plotted in Fig. 14a. The distribution shows a Gaussian shape with a shoulder around  $Z = 52$  revealing the contribution of asymmetric fission. The mean value of  $Z$  is  $\bar{Z} = 45$ . It suggests that  ${}_{90}\text{Th}$  is the mean element undergoing fission. The variance of the  $Z$ -distribution is 7 charge units.

In Fig. 14b the ratio of the mean number of neutrons  $\bar{N}/Z$  for each element is given. The largest mean number of neutrons per element and coherently the largest variances are found around  $Z = 55$ . A mean number of neutrons  $\bar{N} = 63$  is deduced.

The local variance  $\sigma_N^Z$ , plotted on Fig. 14c, increases from 2.5 to almost 5. The presence of the asymmetric fission component is revealed by the maxima at the two peaks of asymmetric fission.

### 4.2 Total cross sections

The fission cross section summed over all isotopes is found to be  $(1.45 \pm 0.15)$  b. However, a few elements are not involved in the analysis, in the region above  $Z = 64$  and below 28. Above  $Z = 64$  the cross section contributing is evaluated to 7 mb [18]. Below  $Z = 28$ , the analysis of M. V. Ricciardi [44] gives a contribution of 72 mb. Thus the total fission cross section amounts to  $(1.53 \pm 0.15)$  b. This value compares well with previous results of direct measurements of fission cross sections  $(1.46 \pm 0.07)$  b and  $(1.48 \pm 0.06)$  b [35,45], respectively. A value of  $(1.52 \pm 0.12)$  b was obtained in a recent measurement at GSI [46]. It is worth noticing that the present technique offers a high degree of selectivity and sensitivity to measure isotopic yields but a lower precision for total cross section measurements than simpler dedicated experiments. If the cross section for evaporation residues of 0.46 b, obtained by summing isotopic values found by J. Taieb in his analysis of the  ${}^{238}\text{U}$  1 A GeV + p reaction [17] is added, a reaction cross section of  $(1.99 \pm 0.17)$  b is obtained. It agrees with the



value of 1.96 b obtained by using the Glauber approach as described by I. J. Karol [42] with updated nuclear-density distributions [47], and with the INCL-calculation 1.94 b [28].

### 4.3 Symmetric and asymmetric fission

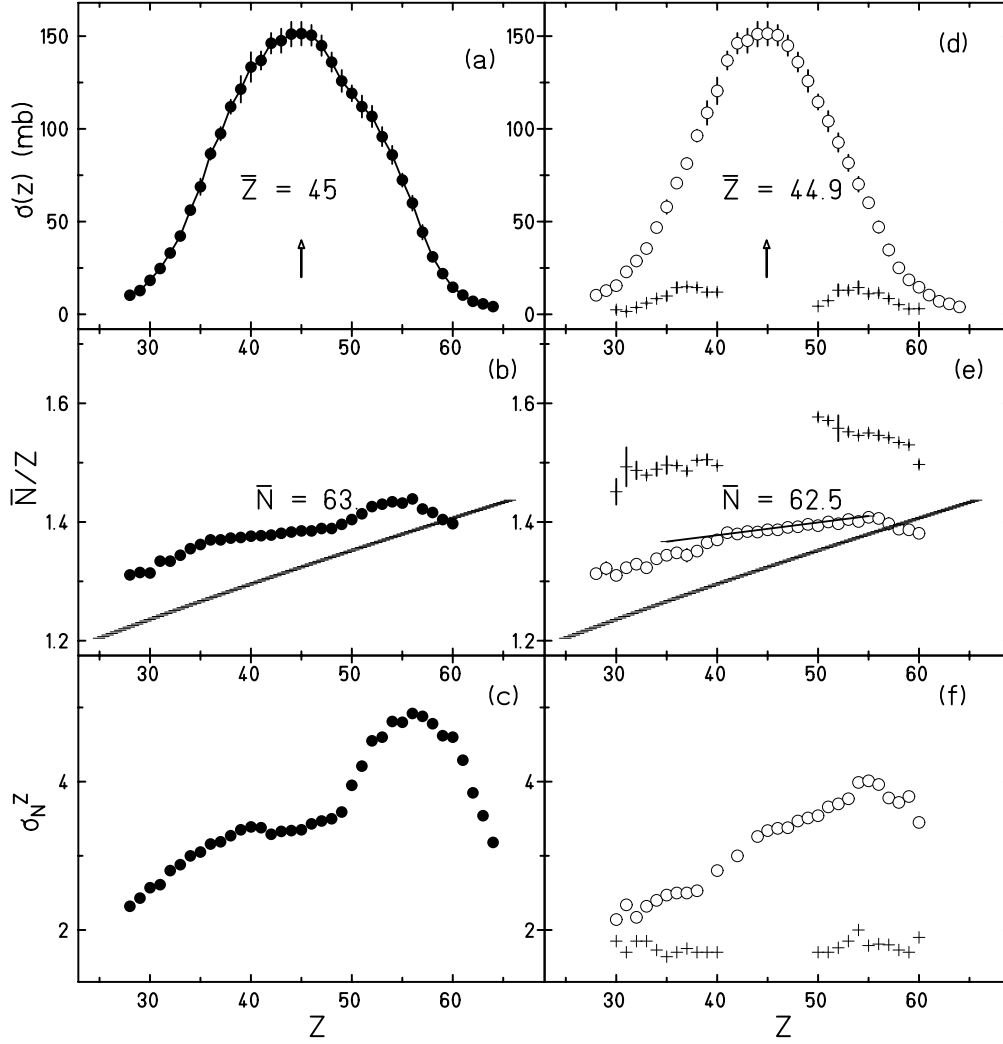


Fig. 14. Integrated distributions of fission fragments from ( $^{238}\text{U} + \text{p}$ ) at 1 A GeV (full points), symmetric fission (empty points) and asymmetric fission (crosses). a) and d):  $Z$ -distribution, b) and e) mean neutron number divided by  $Z$  as a function of  $Z$ , and c) and f) variance in neutron number  $\sigma_N^Z$  for a given  $Z$ . The short line in frame e) corresponds to  $P = -0.04$  [48]. The thick line in frame b) and e) shows the position of the stable isotopes.

The isotopic distributions of elements above  $Z = 50$  can be decomposed into fragments arising from two components: high-excitation symmetric fission and low-excitation asymmetric fission. A decomposition into two Gaussian distri-

butions has been performed, as illustrated in Fig. 15. For the neutron-rich component the mean mass number  $A_p$  and the dispersion  $\sigma_N^Z$  are found to agree with the values known in asymmetric fission, see for example C. Donzaud et al. [20]. For the light fission fragment group, the share of asymmetric fission does not exhibit so clearly and the known values of  $A_p$  and  $\sigma_N^Z$  [20] are used as further inputs.

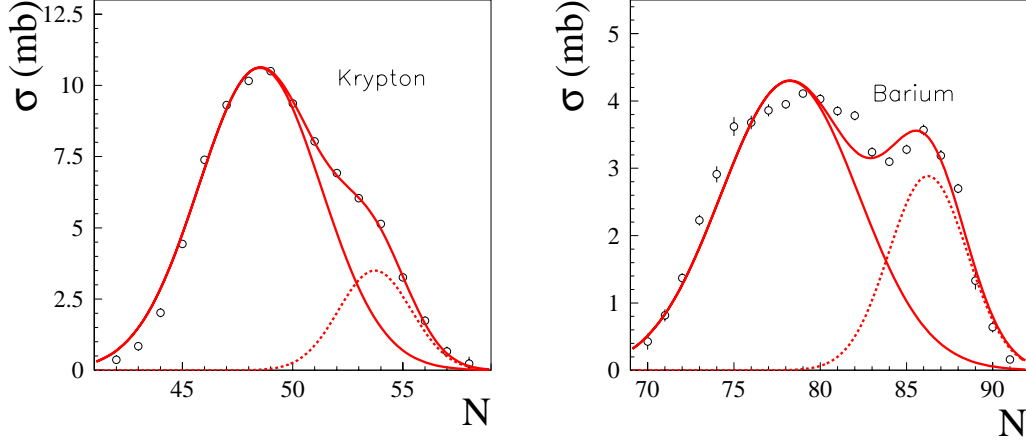


Fig. 15. Examples of the shares of symmetric (full lines) and asymmetric (dotted lines) fission processes. The sum, resulting from the least square fit is indicated.

In spite of the small yields of the asymmetric component, cross sections for the groups of light and heavy fragments are obtained.  $Z$ -integrated cross sections are found the same for the two groups, as to be expected, and equal to  $(105 \pm 10)$  mb. For symmetric fission a cross section of  $(1.42 \pm 0.15)$  b follows. The distribution of elemental cross sections becomes a symmetric curve slightly shifted (empty points in Fig. 14d compared to the total distribution on Fig. 14a). The parameters  $\bar{N} / Z$  and variances  $\sigma_N^Z$  related to the two modes are clearly different. Their values are compatible with two mean primary fissioning nuclei : for the asymmetric mode  $^{234}\text{U}$  and for the symmetric mode  $^{221}\text{Th}$ , with 6 post-scission neutrons added.

The  $\bar{N} / Z$  values of the fragments are not constant , but a slow and regular increment of  $\bar{N} / Z$  with the  $Z$  of the fragment is observed for the high energetic symmetric fission process, see Fig 14e. An electric polarisation  $\delta A_2^{Pol} = -\delta A_1^{Pol} = \bar{A}_2 - Z_2 \times A_0 / Z_0 > 0$  for the fission fragment pairs  $\bar{A}_2, \bar{A}_1$  is indicated. Beyond the regime of nuclear structure dominating asymmetric fission ( $E^* > 40$  MeV) a constant charge polarisability of  $P = -0.04$  is expected [48].  $P$  can be related to the slope of the  $\bar{N} / Z$ -dependence in the range of sym-

metric fission ( $Z_0/Z = 45$ ).

$$P = \frac{-\delta A_2^{pol}(Z)}{A_2 - 0.5A_0} = -(Z_0/2) \times (Z_0/A_0) \times \frac{d(\bar{N}/Z)}{dZ}$$

The thin line in Fig. 14e shows a slope calculated with  $P = -0.04$ .

On Fig. 14f the variance  $\sigma_N^Z$  in the region of symmetric fission increases with the  $Z$ -value of the elements. On the contrary for asymmetric fission, as known for a long time [49], a narrow distribution of isotopes  $\sigma_Z^A$  is populated with a large neutron excess  $\bar{N}/Z$ . Beyond  $Z = 55$  the values of  $\bar{N}/Z$  and of  $\sigma_N^Z$  decrease again and the valley of stability is crossed at  $Z = 58$ . For elements still heavier, fission fragments populate the neutron-deficient side of the valley.

#### 4.4 Mass distribution

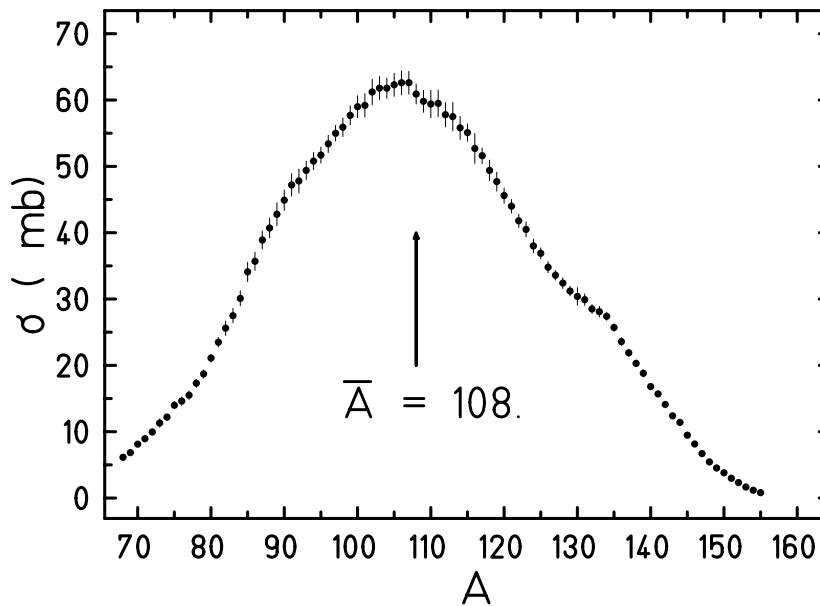


Fig. 16. Mass-distributions of fission fragments for  $^{238}\text{U}$  (1 A GeV) + p.

The mass distribution is obtained by summing isotopic cross sections for a value of  $A$  fixed, Fig. 16. Since isobaric yields do not depend upon  $\beta$ -decay half-lives, mass distribution are accessible also by radiochemical methods and spectroscopic methods [5,6,50]. The distribution shows a wide Gaussian-like shape slightly asymmetric: the slope is steeper on the side of light masses.

The mean mass is  $\bar{A} = 108.0 \pm 0.3$  and the variance of the distribution  $\sigma_A = (17.5 \pm 0.5)$  a.m.u. Enhancements on both sides result from the asymmetric fission component. Since elements below  $Z = 28$  are neglected, which contribute by about 5% to the total cross section [44], the value of  $\bar{A}$  given is

reaction	$\sigma_{sym}$ (barn)	$E_k$ (MeV)	$Z$ (a.ch.u.)	$N$ (a.m.u.)	$\sigma_Z$ (a.ch.u.)	$\sigma_A$ (a.m.u.)	$\sigma_Z^A$ (a.ch.u.)
U + p	1.42±0.2	76±3	45.0±0.1	63.0±0.15	7.0± 0.2	17.5±0.5	1.2±0.1
U + Pb	1.4±0.2	79±2	42.9±0.6	58.1±0.3	6.9±0.7	17.2 ±1.7	1.3±0.3

Table 2

Parameters characterising fission of  $^{238}\text{U}(1 \text{ A GeV}) + \text{p}$  in comparison to the symmetric share of the fission process for  $^{238}\text{U} + \text{Pb}$  at 0.75 AGeV [21]. The small asymmetric contribution in the first system is neglected in evaluating mean values and variances.

slightly larger than the average over all fission fragments produced. We assume that\*\*\* fission proceeds from a mean parent nucleus of mass  $A = 220$  with  $\nu = 6$  the averaged number of emitted neutrons from the symmetric and asymmetric modes. On table 2 the cross sections, mean values of  $A$  and  $Z$ , variances and local variances are presented and compared to the results of symmetric fission in (U + Pb) [21].

#### 4.5 Kinetic energies

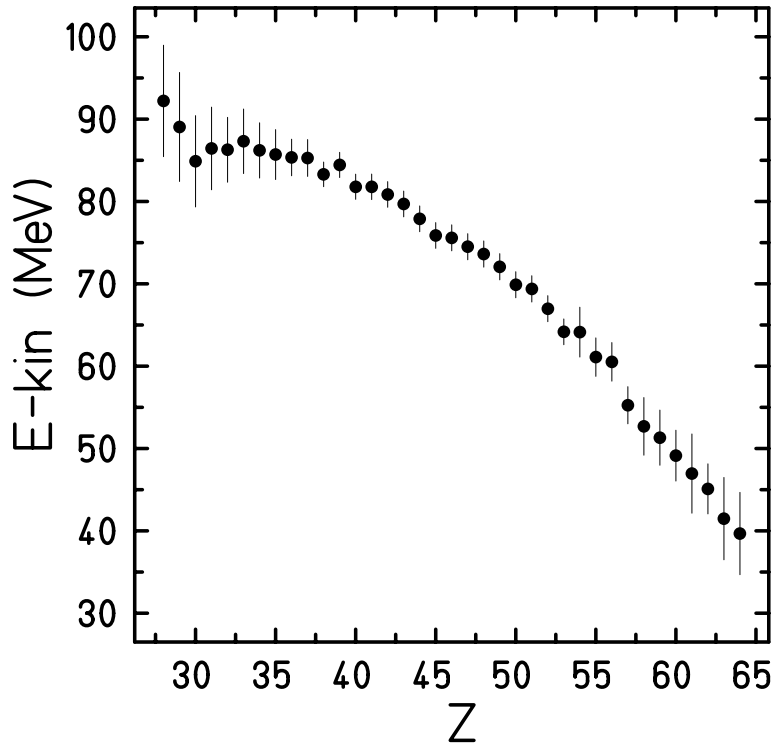


Fig. 17. Mean kinetic energy of fragments from 1 A GeV  $^{238}\text{U} + \text{p}$  fission as a function of their atomic number  $Z$ .

The average kinetic energy of fission fragments as a function of their atomic number is given by  $E_{kin}(Z) = \frac{1}{2} \cdot m_0 \bar{A}(Z) V_f^2$  where  $\bar{A}(Z)$  is the average mass

Z	$E_{kin}$ [MeV]	Z	$E_{kin}$ [MeV]	Z	$E_{kin}$ [MeV]
28	$92.2 \pm 6.8$	41	$81.8 \pm 1.5$	54	$64.1 \pm 3.0$
29	$89.0 \pm 6.6$	42	$80.8 \pm 1.5$	55	$61.1 \pm 2.3$
30	$84.9 \pm 5.5$	43	$79.7 \pm 1.6$	56	$60.5 \pm 2.3$
31	$86.4 \pm 5.0$	44	$77.9 \pm 1.5$	57	$55.2 \pm 2.2$
32	$86.3 \pm 3.9$	45	$75.9 \pm 1.5$	58	$52.7 \pm 3.5$
33	$87.3 \pm 3.9$	46	$75.6 \pm 1.6$	59	$51.3 \pm 3.3$
34	$86.2 \pm 3.3$	47	$74.5 \pm 1.6$	60	$49.1 \pm 3.1$
35	$85.7 \pm 3.0$	48	$73.6 \pm 1.6$	61	$46.9 \pm 4.8$
36	$85.3 \pm 2.2$	49	$72.1 \pm 1.6$	62	$45.1 \pm 3.0$
37	$85.3 \pm 2.2$	50	$69.9 \pm 1.6$	63	$41.5 \pm 5.$
38	$83.3 \pm 1.5$	51	$69.4 \pm 1.6$	64	$39.7 \pm 5.$
39	$84.4 \pm 1.5$	52	$67.0 \pm 1.6$		
40	$81.8 \pm 1.5$	53	$64.2 \pm 1.6$		

Table 3

The mean kinetic energy values of single fission fragments as a function of the atomic number  $Z$ .

number obtained from the measured isotopic distribution, and  $V_f$  is the corresponding fragment velocity as shown in Fig. 9a. The mean kinetic energies are given in table 3 and shown in Fig. 17. They decrease smoothly for higher atomic numbers and show a broad maximum around  $Z = 32$ . The mean value of the kinetic energy, calculated by using the  $Z$ -distribution of Fig. 14a gives  $(76 \pm 3)$  MeV, corresponding to a mean total kinetic energy release of  $(152 \pm 6)$  MeV.

#### 4.6 Comparison with simulation codes

The set of isotopic distributions of fission fragments provides a real challenge for simulation codes. A fast and simple formulation developed by Silberberg and Tsao [51] is shown in Fig. 18 and 19. The model reproduces the orders of magnitude of the isotopic distributions, but the asymmetric fission component is overestimated in magnitude and symmetric components are too narrow. Isotopes of elements at and below  $Z = 35$  are poorly reproduced. A jump at  $Z = 35$  in the code produces the unrealistic gap in the mass distribution at  $A = 90$ .

The second code widely used is the LAHET-code (Los Alamos [24] or Oak Ridge version) [52]. The agreement with this code is not satisfying. In Fig. 18 and 19 the Oak Ridge version has been used for comparison. For neutron-deficient isotopes, cross sections are overestimated, and symmetric fission is underestimated. An odd-even staggering is produced not seen in the experimental data.

Parallel to our experimental program different approaches to new simulation codes are published or are under way. The first reaction step in spallation,

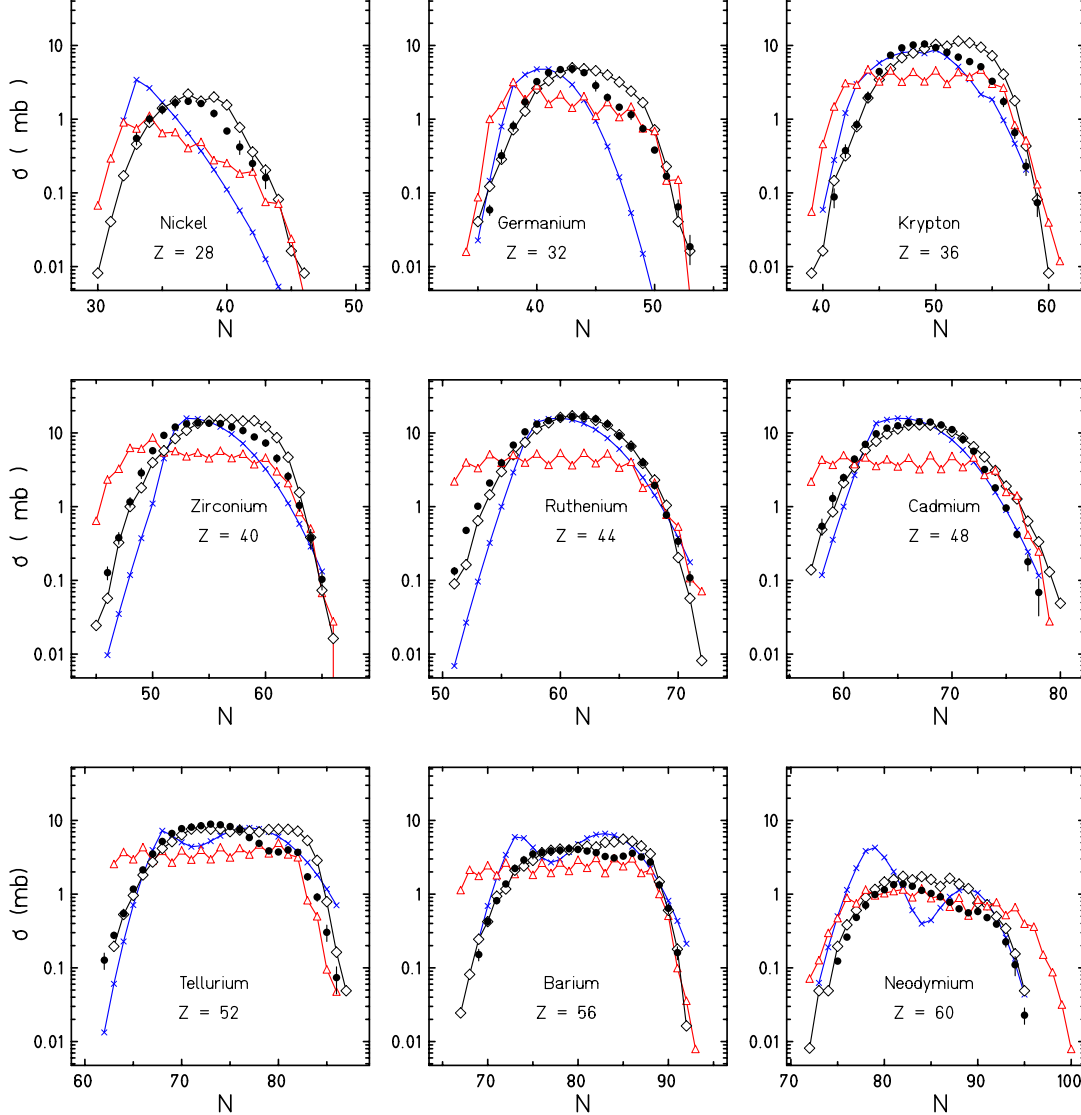


Fig. 18. Comparison of measured isotopic distributions (full points) to calculations with the formula of Silberberg et al. [51] (crosses), by LAHET [52] (triangles), and by our improved codes [25–28] (diamonds) for a selection of elements

the intranuclear cascade induced by the primary proton collision, is simulated by the new version of the code INCL [28]. At this stage, a distribution of prefragment nuclei are predicted with an associated excitation energy and intrinsic spin. This is then the physical input to a system of codes simulating the second step of spallation, the de-excitation phase. New results on the physics of particle evaporation were introduced in the statistical de-excitation code ABLA [25,26] and on fission in the fission code PROF1 [27].

The fission code PROF1 is a semi-empirical Monte-Carlo code which calculates the nuclide distribution of fission fragments. It is theoretically based on the

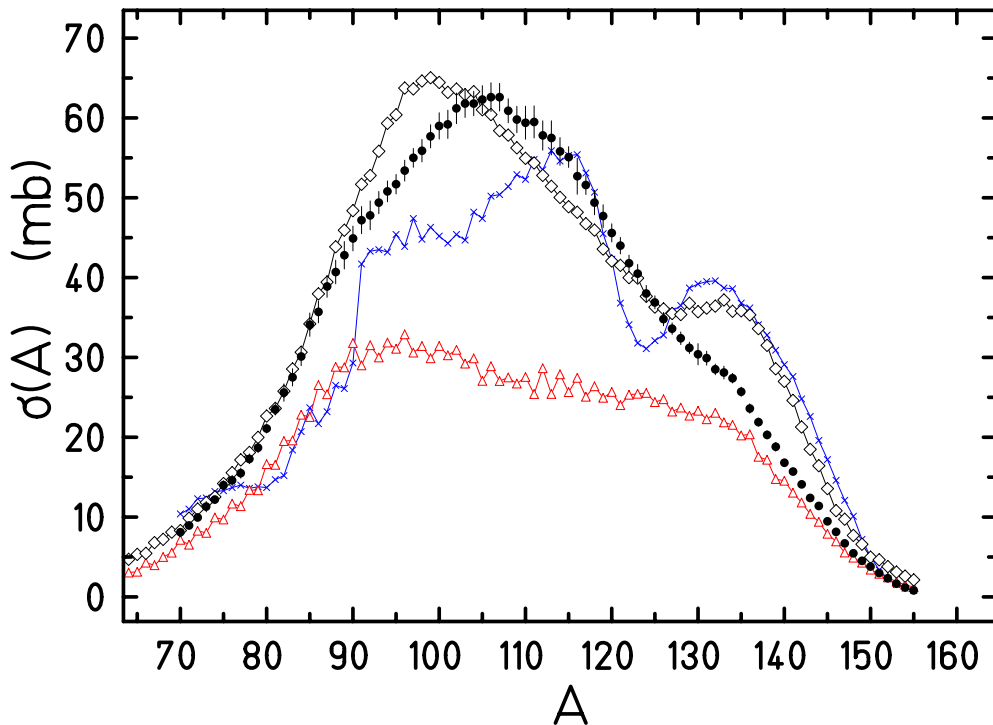


Fig. 19. Mass distribution of fission fragments as a function of mass number compared to simulations; Silberberg [51] (crosses), LAHET [52] (triangle) and to our improved codes [25–28] (diamonds). Experimental data are shown as full symbols with error-bars.

application of the statistical model of nuclear reactions to the concept of fission channels. In this model, the population of the fission channels is assumed to be basically determined by the number of available transition states above the potential energy surface near the fission barrier. Several properties, however, are finally determined at the scission time. A full description of the model is given in [27].

The barrier as a function of mass asymmetry is defined by three components. The first is the symmetric component defined by the liquid-drop potential by means of a parabolic function with a curvature obtained from experimental data [53]. This parabola is assumed to be modulated by two neutron shells, located at mass asymmetries corresponding to neutron numbers  $N = 82$  (spherical neutron shell) and  $N = 90$  (deformed neutron shell). We assume that the mass-asymmetry degree of freedom at the fission barrier is on the average uniquely related to the neutron number of the fragments. The shells are represented by Gaussian functions. These shells are associated with the fission channels Standard I and Standard II, respectively [54], while the liquid-drop potential is associated with the symmetric fission channel. The population of the fission channels is proportional to the level density around the corresponding dips in the potential at saddle at the available excitation energy. Shells are washed out with excitation energy [55]. The heights and the widths of the

Gaussian curves representing the shell effects and additional fluctuations in mass asymmetry acquired from saddle to scission, are derived from experimental data [27]. The mean values of the neutron-to-proton ratio for the channels Standard I and Standard II are deduced from measured nuclide distributions after electromagnetic induced fission of  $^{238}\text{U}$  [20]. The charge polarisation for the symmetric fission channel and the fluctuations in the neutron-to-proton ratio for all channels are also considered by describing the potential in this degree of freedom again by a parabolic function [48]. Assuming that the equilibration in this variable is fast compared to the saddle-to-scission time, this potential was calculated in the scission configuration. Since the shell effects of the nascent fragments at scission, which are strongly deformed on the average, are not known experimentally, only macroscopic properties are included in the calculation of the charge polarisation of the symmetric fission channel.

Consequently, the two fission pre-fragments are obtained. Their excitation energies are calculated from the excitation and deformation energy of the fissioning system at the scission point. The fission probability and the consecutive de-excitation of the fission fragments via particle evaporation are conducted by the routines of the ABLA code [25,26]. Coupling to the cascade code INCL [28] gives a reasonable reproduction of our data, as demonstrated in Fig. 18 and 19 (diamonds). Except for an excess of asymmetric fission the simulation meets the experiment. Either INCL provides a too small excitation energy for the most peripheral collisions, or the excitation energy in the statistical de-excitation chain is underestimated or, finally the parameter set in PROF1 has to be reajusted in order to reduce the share of asymmetric fission.

#### 4.7 *Production of very neutron rich isotopes*

The experimental method of 1 A GeV U-projectile fission opens a very efficient way to produce secondary beams of neutron-rich isotopes. In order to provide experimental cross sections for such a project, the production of very neutron-rich fragments by 1 A GeV U+p collisions is evaluated renormalising the values obtained from a previous dedicated measurement for U+Be [8]. The production of fission fragments differs in both systems because of a relatively larger contribution of asymmetric fission with U + Be. Normalising the elemental cross sections for U + Be to the corresponding element for U + p, the production of very neutron-rich can be deduced reliably down to a level of 1 nb. Not only the falls of the isotopic production with increasing neutron excess are the same for U + Pb and U + Be [20,8], but also the production is found to be the same in the gap of overlapping masses presently covered in U + p.

Fig. 20 illustrates four examples of isotopic distributions. Such exotic beams in spite of their low intensities will be of importance to test predictions for



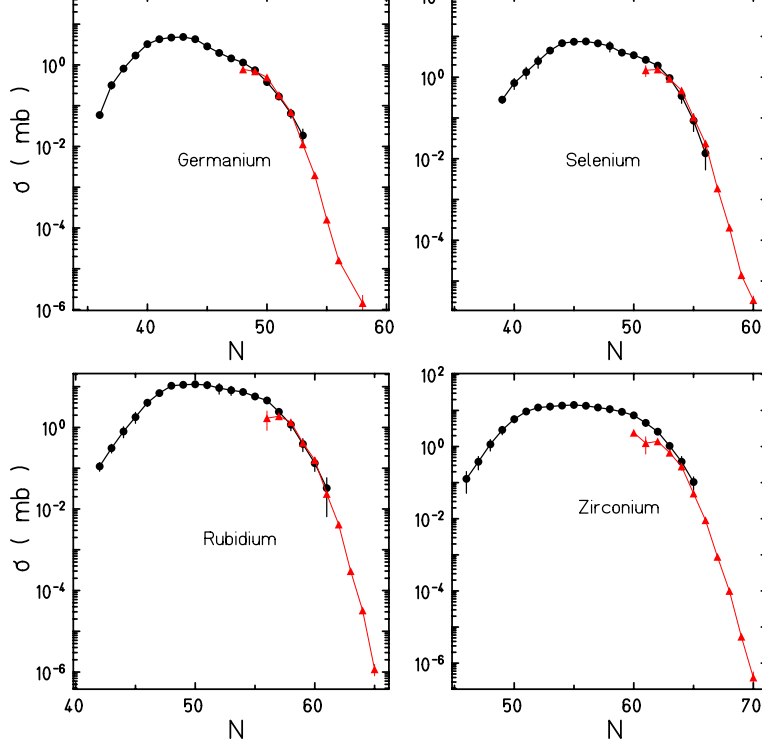


Fig. 20. Comparison of cross-sections from  $^{238}\text{U}$  1 A GeV + p (points) to  $^{238}\text{U}$  0.75 AGeV + Be [8] (triangles). These last data are renormalised in  $\sigma(Z)$  to the present elemental cross sections.

the vanishing of shell-effects at  $N = 82$  and  $50$ , and the possible appearance of neutron halos in the region of tin and nickel isotopes with large neutron excess.

#### 4.8 Parent fissioning nuclei

The reconstitution of the charge  $Z_0$  and mass  $A_0$  of the parent fissioning nuclei is of importance to constrain critical parameters of the intranuclear cascade phase: the transfer of excitation energy and of momentum to the pre-fragments, the value of the density of intermediate states and of the viscosity of highly excited heavy nuclei. The present experimental findings should converge with all other results of  $^{238}\text{U}$  at 1 A GeV + p [17,44,46] on an unified description of a first stage of nucleon-nucleus collision described by a cascade followed by an evaporation stage among which fission occurs.

What is learnt about the fissioning parent nuclei in the present work is listed below:

- Isotopic distributions lead to a mean fission parent nucleus  $^{220}\text{Th}$ .

- For a given element the increase of the mean velocities with the mass of the isotopes (Fig. 8) indicates that parent elements in the range of  $Z_0 \leq 90$  do contribute to the fission.
- Velocities of fragments Fig. 9a show that the region of  $50 \leq Z \leq 64$  arises from parent elements of  $\overline{Z_0} \approx 90$ , while the region of  $30 \leq Z \leq 37$  indicates lower fissioning elements at  $\overline{Z_0} \approx 84$ .
- The variance of the fission fragment velocities  $\sigma_{Vf}$  is extracted from the external slopes of the observed velocity distributions and presented in Fig. 9b. The value of 0.13 cm/ns, the same for all fission-fragment elements, is correlated to the variance of the recoil momenta generated in the nuclear cascade for the ensemble of the fissioning parent nuclei. At  $\Delta A = 18$ , the analysis of spallation presented by J. Taieb [17] gives  $\sigma_p = 350$  MeV/c as the variance of the recoil momenta of the central parent nucleus,  $^{220}\text{Th}$ . This variance is transferred to the fission fragments and leads to a contribution of 0.09 cm/ns in the fissioning system. The ensemble of parent elements and isotopes contributes also by the fluctuations of their TKE-values. A pair of fission-fragments issued from a fixed parent nucleus shows a variance of its velocities. Taking from thermal-neutron induced fission of  $^{235}\text{U}$  the measured value of  $\sigma_{TKE} = 6.0$  MeV as a lower estimate, a contribution of 0.02 cm/ns to the variance of fission fragment velocities is calculated. A much larger contribution is generated by the difference in TKE-values of the many nuclei present. The variance in the  $Z_0$ -distribution of the fissioning parent nuclei of  $\sigma_{Z_0}/Z_0$  of 4.6% is taken from the measurement of B. Jurado [46]. Including the dispersion due to a spread over several isotopes in each element, and converting TKE-values into fragment-velocities, the contribution of the fissioning ensemble is evaluated to 0.09 cm/ns. The location straggling in the thin  $\text{H}_2$ -target induces a negligible contribution of 0.01 cm/ns to this variance. Adding quadratically all contributions, a total variance of 0.13 cm/ns is obtained which coincides with the value extracted from the observed velocity distributions.
- The mean recoil velocities of the parent fissioning nuclei arise from the first phase of the reaction and contribute to the momentum losses measured [17]. The transferred momentum of -150 MeV/c measured for the evaporation residues at  $\Delta A = 18$  should be close to the momentum of the mean fissioning parent  $^{220}\text{Th}$ . This recoil momentum is equivalent to a recoil velocity of -0.04 cm/ns, indicated by a line in Fig. 9c. The recoil velocities presented in Fig. 9c, in the range of -(0.04-0.13) cm/ns are on the average larger by a factor of 2 and show a trend towards larger values for lighter elements.

#### 4.9 Comparison of system $U + p$ and $Pb + p$

Fig. 21 and Table 4 demonstrate the basic difference between the collision systems  $Pb + p$  and  $U + p$ . Both reactions have nearly the same reaction

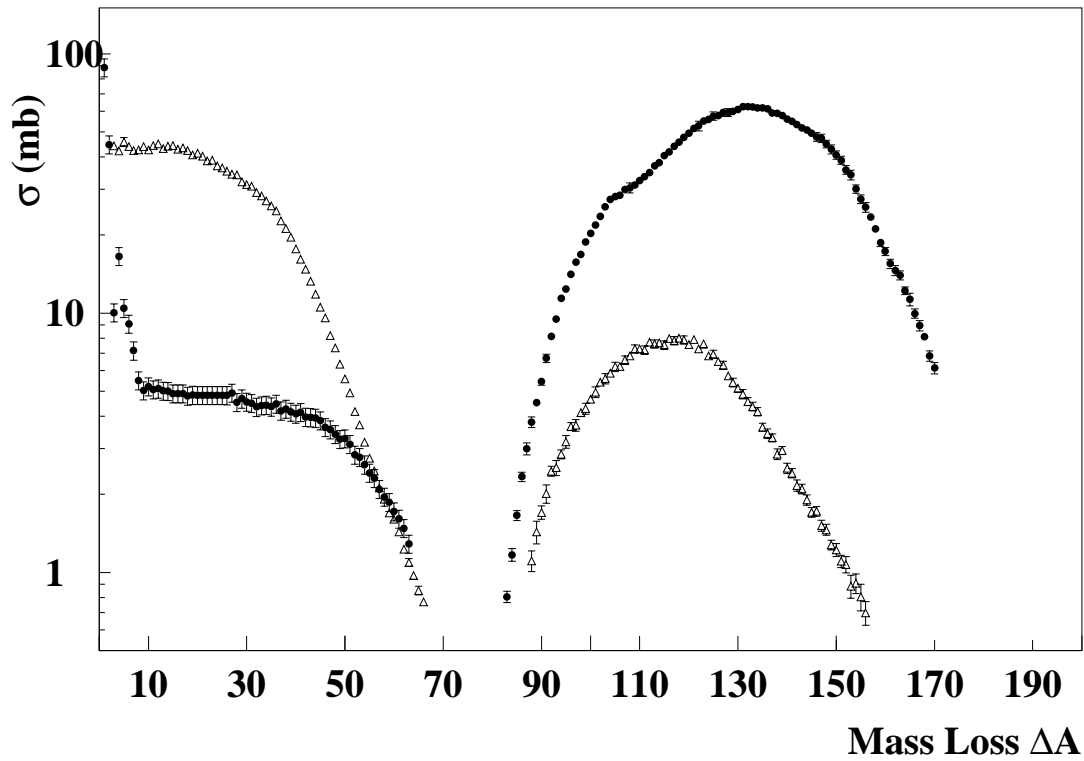


Fig. 21. Comparison of cross-sections for evaporation and fission residues as a function of the mass-loss  $\Delta A$  for the two collision systems Pb + p (triangles) and U + p (full points) at 1 A GeV.

reaction	$\sigma_{tot}$ (barn)	$\sigma_{fis}$ (barn)	$\sigma_{EVR}$ (barn)
U + p	$1.99 \pm 0.17$	$1.53 \pm 0.13$	$0.46 \pm 0.08$
Pb + p	$1.84 \pm 0.23$	$0.16 \pm 0.07$	$1.68 \pm 0.22$

Table 4

Comparison of reaction cross sections of 1 A GeV  $^{238}\text{U} + \text{p}$  to 1 A GeV  $^{208}\text{Pb} + \text{p}$  [15].

cross section, 1.84 b for Pb + p and 1.99 b for U + p. Fragmentation is the main reaction channel for Pb+p, with  $\sigma = (1.68 \pm 0.2)$  b, whereas fission dominates the U+p reaction with a cross section  $\sigma = (1.53 \pm 0.15)$  b.

Averaging over all cross sections from evaporation and fission residues, altogether a mean neutron number of  $127 \pm 1$  is found for reaction products of  $^{238}\text{U} + \text{p}$  at 1 A GeV, i.e.  $19 \pm 1$  neutrons are liberated in the reaction. This number does not include neutrons bound in the lightest elements ( $Z \leq 7$ ), and should be an upper limit for the number of neutrons produced in thin targets. It compares with the neutron multiplicity of 20 measured with 1.2

## 5 Conclusions

We have measured isotopic production cross-sections for about 733 fission fragments produced in 1 A GeV  $^{238}\text{U} + \text{p}$  collisions with a mean accuracy of 10 %, down to values of  $20 \mu\text{b}$  for neutron-rich and 0.1 mb for neutron-deficient isotopes. The population of isotopes resulting from fission is pictured in Fig. 22 on the chart of nuclei. The isobaric slope of the production cross section towards the neutron rich side of the chart of isotopes is found to be the same for hydrogen as for heavier targets investigated earlier.

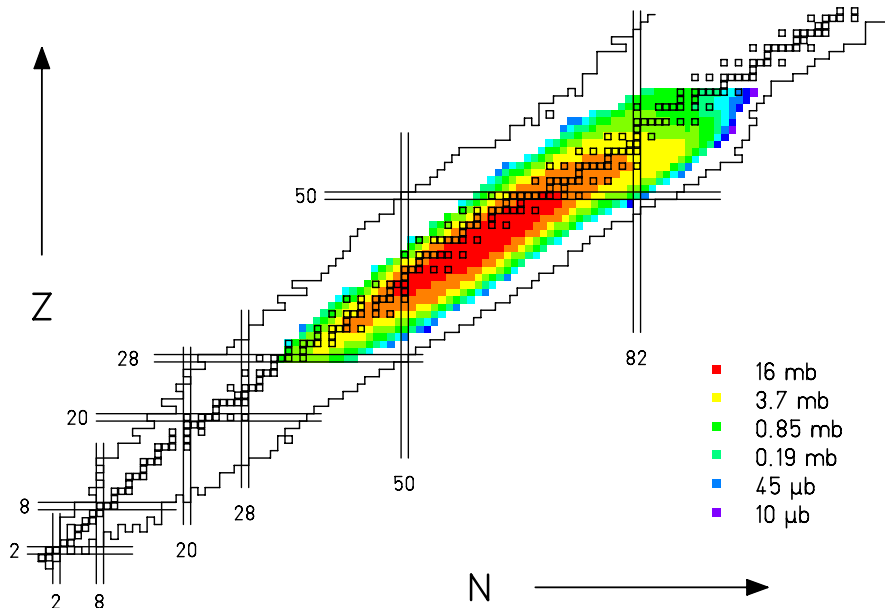


Fig. 22. Two-dimensional plot of the isotopic cross sections for fission-fragments obtained in 1 A GeV  $^{238}\text{U} + \text{p}$  shown on the chart of isotopes with squares indicating stable isotopes. Colours correspond to increasing cross sections according to the logarithmic scale indicated.

The fission cross section, including the production of very light elements, amounts to  $(1.53 \pm 0.15)$  b which compares well with previous results [35,45] as with the recent result of B. Jurado [46]. The total cross section of fission plus evaporation residues amounts to  $(1.99 \pm 0.17)$  b, close to the calculated geometrical cross section of 1.96 b [42,47] and to the INCL calculation 1.94 b [28].

Our results show a good quantitative agreement with previous isotopic distributions of cross sections measured for rubidium and cesium with on-line mass-separator techniques except for a discrepancy in cross sections for the 6 most neutron-rich isotopes of cesium [3]. The coherence of the present experimental method validates our mass-calibration relatively to all other isotopes. Parameters characterising fission and its variances are extracted. The elemental distribution and the kinetic energies of the reaction products are of importance concerning chemical corrosion and the composition of nuclear waste produced by spallation of actinides.

The analysis of the momentum and velocity spectra of fission-fragments as function of  $A$  and  $Z$  gives an indication on the nature and the domain of excitation energies of the fragments arising from the first step of the  $(U + p)$ -interaction and undergoing fission. Comparison with previous measurements shows that the symmetric fission cross section  $(1.42 \pm 0.20)$  b is almost the same for  $U + p$  as for  $U + Pb$ ,  $(1.4 \pm 0.2)$  b. In this last case the first phase of violent abrasion leads to a wider range of more excited and lighter fragments. The fission probabilities of these fragments are smaller than for actinides close to the  $U$ -projectiles which are mainly produced in  $(U + p)$ -collisions. Finally the cross section to observe symmetric fission remains the same for both systems.

There is certainly not a perfect overlap between the distribution of fragments identified as evaporation-residues and the fissioning parent nuclei. The parent nuclei close to  $U$  have high fissilities. For elements of decreasing  $Z$  numbers, fissile isotopes become more and more neutron-deficient. Compared to the evaporation-residues the fissioning-parent nuclei are shifted towards the neutron-deficient side. They are born from prefragments of higher excitation energies and their recoil momenta may be higher than for those ending as evaporation residues.

Measured isotopic and mass distributions are compared to results obtained with simulation codes commonly used. Large discrepancies are shown, and the need for improved reaction models is underlined. Models developed recently in the collaboration are discussed [25–28] and the improvements achieved are demonstrated.

## 6 Acknowledgements

We wish to thank F. Ameil, K. Günzer and M. Pravikoff for their participation to the data taking and K. H. Behr, A. Brünle and K. Burkard for their technical support during the experiment. We are thankful to the group of P. Chesny who built the liquid-hydrogen target. We thank O. Yordanov and A. Kelic for their help and interest in the late stage of our work. This work was partially

## 7 Appendix 1

### 7.1 Demonstration of equations (7) and (8)

The transformation from the c.m.-system to the lab-system is given by:

$$\gamma \tan \phi = \frac{\beta_f \sin \varphi}{\beta_0 \pm \beta_f \cos \varphi} \quad (11)$$

with  $\pm$  signs for forward and backward angles  $\varphi^F$  and  $\varphi^B$ , respectively. To transform back to the c.m.-system for the limiting case  $\phi_{lim} = \alpha$ , we solve equ. (11) for this case:

$$\gamma \tan \alpha = \frac{\sin \varphi}{K \pm \cos \varphi} \quad (12)$$

with  $K = \beta_0 / \beta_f$ . It is convenient to solve equ. (12) as a quadratic equation in  $\tan(\varphi/2)$ , which has 2 solutions corresponding to  $\varphi^F$  and  $\varphi^B$  given for  $\phi_{lim} = \alpha$  in the lab-system.

$$\tan(\varphi^{F,B}/2) = \frac{K \pm 1}{\sqrt{K^2 - 1}} \tan \delta/2 \quad (13)$$

with an auxiliary variable

$$\sin \delta = \gamma \sqrt{K^2 - 1} \tan \alpha \quad (14)$$

Equ. 13 shows that the angles  $\varphi^F$  and  $\varphi^B$  depend via eq. (14) on all 3 variables  $\alpha$ ,  $\beta_0$  and  $\beta_f$ . The transmission of each of the cones may be evaluated with the total transmission obtained by summing  $T_\Omega^F$  and  $T_\Omega^B$ . This method we applied in our evaluations until now [13,15,16]. However, introducing the two solutions of equ. (13) into equ. (3) we obtain another very compact expression for  $T_\Omega$ :

$$T_\Omega = 1 - \frac{\cos \delta}{1 + (\gamma \tan \alpha)^2} \quad (15)$$

Equ. (15) depends via the auxiliary variable  $\delta$  on the fission velocity. To illuminate the variable  $\delta$  we introduce  $\varphi_\Sigma = (\varphi^F + \varphi^B)/2$  and  $\varphi_\Delta = (\varphi^F -$

$\varphi = \varphi_{\Sigma} + \varphi_{\Delta}$  and  $\varphi = \varphi_{\Sigma} - \varphi_{\Delta}$ . Equ. (15) transforms to the new variables using the trigonometrical sum relations for  $\tan \varphi_{\Sigma}$  and  $\tan \varphi_{\Delta}$ .

$$\tan \varphi_{\Sigma} = \frac{K}{\sqrt{K^2 - 1}} \tan \delta \tan \varphi_{\Delta} = \gamma \tan \alpha \quad (16)$$

Angle  $\varphi_{\Delta}$  depends only on two variables,  $\gamma$  and  $\alpha$ , which represent the relativistic beam and the FRS spectrometer. The fission velocity  $\beta_f$  enters into the angle  $\varphi_{\Sigma}$ . Between  $\varphi^{F,B}$  and  $\varphi_{\Sigma,\Delta}$  another trigonometrical relation holds

$$\cos \varphi^F + \cos \varphi^B = 2 \cos \varphi_{\Sigma} \cos \varphi_{\Delta}$$

This relation introduced in equ. (3) gives for the transmission :

$$T_{\Omega} = 1 - \cos \varphi_{\Sigma} \cos \varphi_{\Delta} \quad (17)$$

Comparing equ. (15) and (18) a relation between  $\varphi_{\Sigma,\Delta}$  and  $\delta$  follows:

$$\cos \delta = \frac{\cos \varphi_{\Sigma}}{\cos \varphi_{\Delta}} = \cos \varphi_{\Sigma} \sqrt{1 + (\gamma \tan \alpha)^2}$$

The three expressions equ. (3),(15) and (18) are exact, identical representations in different angular coordinates. All expressions derived for the transmission until now depend on  $\beta_f$ . The conversion of  $\beta_f$  into the measured quantity  $\beta_{app}$  makes use of equ. (6) and (14) :

$$\sin \delta = \frac{\sqrt{\beta_0^2 - \beta_f^2}}{\beta_f} \gamma \tan \alpha = \frac{\sqrt{\beta_0^2 - \beta_f^2} \gamma \tan \alpha}{2\beta_{app}} (2 - T_{\Omega}) \quad (18)$$

Also equ. (6) and (19) are exact without any approximations.

For our experiment with  $\gamma = 2.07$  and  $\alpha = \bar{\alpha} = 14.8$  mrad,  $\varphi_{\Sigma}$  is larger than  $\delta$  by only 0.1 mrad. It is a good approximation to replace  $\varphi_{\Sigma}$ , the mean value of  $\varphi^F$  and  $\varphi^B$ , by the auxiliary variable  $\delta$ . A next approximation for the transmission follows:

$$T_{\Omega} = 1 - \cos \varphi_{\Sigma} \quad (19)$$

which deviates from the exact value by less than 0.2 % in the worst case of  $Z = 28$ . Neglecting terms in  $\alpha^2$  and  $K^{-2}$  useful approximations derived from eqs (16) and (17) are:

$\varphi_{\Sigma} = \theta$  and  $\varphi_{\Delta} = \gamma\alpha$

$$\varphi^F = \varphi_{\Sigma} + \gamma\alpha \text{ and } \varphi^B = \varphi_{\Sigma} - \gamma\alpha$$

From equ. (20) and (6) we derive equ. (7) and (8).

With  $\beta_{lim} \equiv \alpha \sqrt{\gamma^2 - 1}$  follows:

$$\tan \varphi_{\Sigma}/2 = \frac{\alpha \sqrt{\gamma^2 - 1}}{2\beta_{app}} = \frac{\beta_{lim}}{2\beta_{app}} \quad (20)$$

Finally with equ. (21)  $\beta_f$  and  $T_{\Omega}$  can be presented as a function of  $\beta_{app}$ , see equ. (7) and (8) given in section 2.5.

$$T_{\Omega} = \frac{2}{1 + [2\beta_{app}/\beta_{lim}]^2}$$

and

$$\beta_f = \beta_{app}[1 + (\beta_{lim}/2\beta_{app})^2]$$

q. e. d.



Z	A	$\sigma$ [mb]
28	61	0.55 (10)
	62	1.00 (14)
	63	1.35 (17)
	64	1.67 (20)
	65	1.75 (15)
	66	1.67 (11)
	67	1.20 (13)
	68	0.69 (5)
	69	0.42 (8)
	70	0.25 (4)
	71	0.16 (3)
29	63	0.49(12)
	64	0.89(16)
	65	1.24(19)
	66	1.70(17)
	67	2.01(15)
	68	2.08(13)
	69	1.64(13)
	70	1.20(8)
	71	0.67(12)
	72	0.39(4)
	73	0.23(2)
74	0.11(5)	
30	64	0.13(3)
	65	0.46(7)
	66	0.94(13)
	67	1.52(21)
	68	2.41(20)
	69	2.86(17)
	70	3.00(9)
	71	2.54(20)
	72	1.95(23)
	73	1.27(10)
	74	0.88(7)
	75	0.54(3)
	76	0.26(3)
77	0.12(2)	
78	0.047(21)	
31	67	0.36(10)
	68	0.90(18)
	69	1.60(20)
	70	2.87(14)

	71	3.58(21)
	72	3.68(22)
	73	3.60(54)
	74	2.99(18)
	75	2.16(37)
	76	1.22(17)
	77	0.82(7)
	78	0.55(9)
	79	0.30(2)
	80	0.14(3)
	81	0.033(14)
32	69	0.32(6)
	70	0.81(13)
	71	1.71(26)
	72	3.24(23)
	73	4.28(21)
	74	4.70(28)
	75	4.83(18)
	76	4.28(30)
	77	2.85(45)
	78	1.97(22)
	79	1.45(10)
	80	1.15(16)
	81	0.74(6)
	82	0.38(2)
	83	0.17(1)
	84	0.065(15)
	85	0.019(8)
33	71	0.29(8)
	72	0.70(14)
	73	1.63(26)
	74	2.84(28)
	75	5.01(30)
	76	5.93(36)
	77	6.10(30)
	78	5.33(32)
	79	4.50(27)
	80	3.34(30)
	81	2.62(13)
	82	1.88(17)
	83	1.36(13)
	84	0.74(11)
	85	0.36(4)
	86	0.16(2)
	87	0.03(20)
34	73	0.28 (5)
	74	0.70 (14)

	75	1.30 (21)
	76	2.42 (39)
	77	4.42 (26)
	78	6.68 (27)
	79	7.25 (43)
	80	7.37 (29)
	81	6.64 (46)
	82	5.67(80)
	83	3.93(24)
	84	3.41(14)
	85	2.61(18)
	86	1.88(11)
	87	0.93 (9)
	88	0.34 (6)
	89	0.085 (25)
35	75	0.19(7)
	76	0.52 (10)
	77	1.08(20)
	78	2.37(38)
	79	4.22(34)
	80	6.79(20)
	81	8.23(33)
	82	8.49(51)
	83	8.02(77)
	84	7.23(72)
	85	6.13(86)
	86	4.66(56)
	87	3.80(15)
	88	2.92(23)
	89	1.95(19)
	90	0.75(10)
	91	0.25(6)
	92	0.06(2)
36	77	0.09(3)
	78	0.37(7)
	79	0.84(13)
	80	2.0(3)
	81	4.43(40)
	82	7.40(44)
	83	9.31(56)
	84	10.2(7)
	85	10.5(9)
	86	9.36(94)
	87	8.04(96)
	88	6.92(69)
	89	6.03(36)
	90	5.14(31)

	91	3.26(16)
	92	1.74(26)
	93	0.66(11)
	94	0.23(6)
	95	0.07(2)
37	79	0.11(3)
	80	0.31(6)
	81	0.80(13)
	82	1.80(29)
	83	4.05(40)
	84	6.93(41)
	85	10.5(5)
	86	11.2(6)
	87	11.4(6)
	88	11.0(10)
	89	9.2(14)
	90	8.2(11)
	91	7.4(6)
	92	6.12(61)
	93	4.6(2)
	94	2.4(2)
	95	1.17(18)
	96	0.39(7)
	97	0.13(3)
	98	0.031(16)
38	83	0.63(18)
	84	1.58(27)
	85	3.50(52)
	86	7.02(49)
	87	11.1(6)
	88	11.8(6)
	89	12.0(6)
	90	11.9(7)
	91	12.2(12)
	92	10.2(12)
	93	9.05(61)
	94	8.24(50)
	95	6.1(5)
	96	4.36(26)
	97	2.14(32)
	98	0.88(18)
	99	0.24(4)
	100	0.069(14)
39	85	0.51(14)
	86	1.36(27)
	87	3.21(45)
	88	6.51(52)

	89	10.3(5)
	90	12.1(6)
	91	12.4(7)
	92	12.5(9)
	93	12.4(9)
	94	11.4(7)
	95	10.5(5)
	96	8.75(44)
	97	7.36(37)
	98	5.62(67)
	99	3.81(27)
	100	1.65(26)
	101	0.68(17)
	102	0.19(6)
	103	0.04(2)
40	86	0.127(25)
	87	0.377(68)
	88	1.15(17)
	89	2.86(46)
	90	5.73(45)
	91	9.30(74)
	92	12.0(5)
	93	13.3(7)
	94	13.7(7)
	95	13.5(7)
	96	13.4(8)
	97	12.0(13)
	98	10.8(11)
	99	8.80(44)
	100	7.30(73)
	101	4.50(58)
	102	2.57(36)
	103	1.04(18)
	104	0.38(11)
	105	0.10(3)
41	89	0.30(7)
	90	1.05(21)
	91	2.38(38)
	92	4.55(55)
	93	7.56(38)
	94	10.5(4)
	95	12.6(5)
	96	13.7(5)
	97	14.5(6)
	98	14.4(9)
	99	13.3(8)
	100	11.9(8)

	104	2.92(50)
	105	1.56(44)
	106	0.55(16)
	107	0.19(10)
42	92	0.72(19)
	93	1.81(27)
	94	3.58(43)
	95	6.24(37)
	96	9.68(48)
	97	12.8(8)
	98	14.0(7)
	99	15.1(8)
	100	16.2(10)
	101	15.7(11)
	102	14.9(12)
	103	13.0(8)
	104	9.91(49)
	105	6.18(43)
	106	3.96(20)
	107	1.78(19)
	108	0.91(27)
	109	0.28(7)
	110	0.08(4)
43	94	0.68(12)
	95	1.36(31)
	96	2.69(30)
	97	5.02(35)
	98	8.11(40)
	99	11.5(7)
	100	13.3(7)
	101	15.2(8)
	102	15.9(10)
	103	16.2(11)
	104	15.8(9)
	105	14.4(11)
	106	11.6(9)
	107	8.44(51)
	108	4.88(34)
	109	2.90(20)
	110	1.31(26)
	111	0.60(18)
	112	0.17(8)
44	95	0.13(2)
	96	0.47(4)
	97	1.01(7)
	98	2.10(17)
	99	3.91(23)

	100	6.84(34)
	101	8.77(60)
	102	13.1(8)
	103	14.7(7)
	104	16.0(8)
	105	16.7(10)
	106	16.6(13)
	107	15.4(11)
	108	13.1(7)
	109	9.17(46)
	110	6.62(40)
	111	3.95(31)
	112	1.94(21)
	113	0.77(8)
	114	0.34(5)
	115	0.11(2)
45	99	0.70(9)
	100	1.52(8)
	101	3.00(15)
	102	5.28(37)
	103	8.62(60)
	104	11.5(6)
	105	14.2(6)
	106	15.4(4)
	107	16.6(10)
	108	16.3(10)
	109	15.7(9)
	110	13.6(14)
	111	11.7(6)
	112	8.11(4)
	113	5.11(25)
	114	2.60(10)
	115	1.40(5)
	116	0.54(7)
	117	0.20(10)
46	100	0.19(2)
	101	0.54(3)
	102	1.21(6)
	103	2.48(12)
	104	4.36(17)
	105	7.33(29)
	106	10.7(7)
	107	13.0(6)
	108	14.5(6)
	109	15.2(9)
	110	16.2(13)
	111	15.8(16)

	112	14.8(12)
	113	12.6(9)
	114	9.58(38)
	115	6.25(25)
	116	3.57(14)
	117	1.91(27)
	118	0.93(11)
	119	0.37(10)
	120	0.12(2)
47	103	0.40(4)
	104	0.86(5)
	105	1.81(9)
	106	3.19(16)
	107	5.73(23)
	108	8.40(34)
	109	11.4(8)
	110	12.6(5)
	111	14.0(7)
	112	14.5(10)
	113	16.0(17)
	114	14.5(13)
	115	13.5(8)
	116	10.5(14)
	117	7.73(31)
	118	4.74(19)
	119	2.64(18)
	120	1.38(8)
	121	0.65(3)
	122	0.22(3)
	123	0.07(1)
48	106	0.54(13)
	107	1.30(26)
	108	2.47(30)
	109	4.41(44)
	110	7.00(35)
	111	9.75(58)
	112	11.6(8)
	113	12.5(5)
	114	13.7(7)
	115	14.2(6)
	116	14.0(6)
	117	12.8(6)
	118	11.1(4)
	119	8.21(33)
	120	5.64(23)
	121	3.20(20)
	122	1.80(13)



	123	0.96(10)
	124	0.42(5)
	125	0.18(4)
	126	0.069(34)
49	107	0.14(3)
	108	0.34(5)
	109	0.77(8)
	110	1.71(22)
	111	3.15(41)
	112	5.26(47)
	113	7.78(70)
	114	10.0(8)
	115	11.3(7)
	116	12.0(10)
	117	13.0(8)
	118	13.0(13)
	119	12.7(9)
	120	11.0(7)
	121	9.22(37)
	122	6.16(24)
	123	3.98(16)
	124	2.27(9)
	125	1.38(8)
	126	0.75(6)
	127	0.41(6)
	128	0.19(3)
	129	0.08(2)
	130	0.02(1)
50	110	0.23(2)
	111	0.56(6)
	112	1.26(13)
	113	2.39(24)
	114	4.09(20)
	115	6.38(25)
	116	8.6(13)
	117	9.97(40)
	118	10.4(4)
	119	11.0(4)
	120	11.5(5)
	121	11.6(5)
	122	10.5(4)
	123	9.28(37)
	124	6.77(27)
	125	4.82(20)
	126	2.90(11)
	127	2.00(8)
	128	1.56(6)

	129	1.29(5)
	130	1.01(7)
	131	0.66(7)
	132	0.35(7)
	133	0.05(3)
51	112	0.16(6)
	113	0.36(9)
	114	0.82(12)
	115	1.66(25)
	116	2.97(23)
	117	4.66(28)
	118	6.6(5)
	119	8.3(9)
	120	9.1(5)
	121	9.59(57)
	122	10.2(5)
	123	10.6(8)
	124	10.2(5)
	125	9.3(5)
	126	7.63(45)
	127	5.67(28)
	128	3.88(31)
	129	2.87(14)
	130	2.43(12)
	131	2.46(29)
	132	1.85(27)
	133	1.27(23)
	134	0.42(25)
	135	0.12(5)
52	114	0.12(3)
	115	0.27(3)
	116	0.54(4)
	117	1.16(8)
	118	2.11(17)
	119	3.48(31)
	120	5.1(5)
	121	6.61(53)
	122	7.7(6)
	123	8.02(48)
	124	8.40(42)
	125	8.80(35)
	126	8.61(34)
	127	8.18(33)
	128	7.40(30)
	129	5.79(35)
	130	4.84(29)
	131	3.83(23)

	132	3.70(22)
	133	3.94(39)
	134	3.64(22)
	135	1.70(17)
	136	0.90(11)
	137	0.30(8)
	138	0.074(30)
53	116	0.06(1)
	117	0.17(3)
	118	0.45(7)
	119	0.82(8)
	120	1.49(10)
	121	2.50(15)
	122	3.9(4)
	123	5.4(5)
	124	6.3(7)
	125	6.8(4)
	126	7.30(44)
	127	7.60(30)
	128	7.81(39)
	129	7.54(30)
	130	6.90(35)
	131	6.06(36)
	132	4.91(24)
	133	4.38(31)
	134	4.09(20)
	135	4.32(21)
	136	3.08(28)
	137	2.29(21)
	138	1.21(12)
	139	0.53(13)
	140	0.16(3)
	141	0.038(8)
54	118	0.032(9)
	119	0.118(18)
	120	0.25(2)
	121	0.51(5)
	122	1.01(7)
	123	1.82(9)
	124	2.91(17)
	125	4.17(25)
	126	4.99(40)
	127	5.68(45)
	128	5.88(41)
	129	6.14(37)
	130	6.27(38)
	131	6.39(45)

	132	6.01(18)
	133	5.43(33)
	134	5.05(30)
	135	4.66(23)
	136	4.48(27)
	137	4.05(16)
	138	3.96(20)
	139	3.15(31)
	140	2.11(25)
	141	0.77(9)
	142	0.32(4)
	143	0.06(2)
55	122	0.12(3)
	123	0.27(4)
	124	0.69(8)
	125	1.27(13)
	126	2.05(8)
	127	3.03(15)
	128	3.98(32)
	129	4.60(32)
	130	4.86(24)
	131	4.94(15)
	132	5.05(25)
	133	5.24(26)
	134	5.19(15)
	135	4.74(24)
	136	4.43(22)
	137	3.89(27)
	138	3.33(20)
	139	3.55(21)
	140	3.34(20)
	141	3.40(13)
	142	2.05(8)
	143	1.04(3)
	144	0.40(4)
	145	0.12(2)
56	125	0.16(3)
	126	0.42(5)
	127	0.82(8)
	128	1.37(9)
	129	2.23(17)
	130	2.91(34)
	131	3.50(50)
	132	3.68(37)
	133	3.86(34)
	134	3.95(24)
	135	4.11(21)

	136	4.03(20)
	137	3.85(20)
	138	3.65(29)
	139	3.24(22)
	140	3.10(18)
	141	3.28(23)
	142	3.57(28)
	143	3.19(16)
	144	2.70(19)
	145	1.33(17)
	146	0.65(10)
	147	0.16(3)
57	127	0.10(3)
	128	0.22(6)
	129	0.55(8)
	130	0.99(10)
	131	1.56(14)
	132	2.16(17)
	133	2.73(22)
	134	3.12(19)
	135	3.24(23)
	136	3.22(22)
	137	3.21(16)
	138	3.17(16)
	139	2.97(24)
	140	2.49(15)
	141	2.24(16)
	142	2.23(16)
	143	2.20(18)
	144	2.27(20)
	145	2.31(18)
	146	1.88(15)
	147	1.25(19)
	148	0.53(11)
	149	0.20(5)
	150	0.03(1)
58	130	0.17(6)
	131	0.33(6)
	132	0.61(5)
	133	0.96(9)
	134	1.52(9)
	135	1.96(20)
	136	2.20(20)
	137	2.34(16)
	138	2.34(14)
	139	2.28(11)
	140	2.27(11)

	141	2.08(12)
	142	1.82(9)
	143	1.60(10)
	144	1.52(9)
	145	1.45(10)
	146	1.45(9)
	147	1.33(9)
	148	1.19(10)
	149	0.75(4)
	150	0.44(4)
	151	0.11(4)
	152	0.02(1)
59	131	0.053(13)
	132	0.104(21)
	133	0.214(38)
	134	0.362(36)
	135	0.69(10)
	136	1.09(11)
	137	1.41(10)
	138	1.66(12)
	139	1.77(11)
	140	1.73(14)
	141	1.69(8)
	142	1.59(8)
	143	1.50(9)
	144	1.43(7)
	145	1.26(9)
	146	1.13(12)
	147	0.94(10)
	148	0.84(7)
	149	0.88(7)
	150	0.73(7)
	151	0.54(3)
	152	0.27(2)
	153	0.066(19)
	154	0.012(6)
60	135	0.12(1)
	136	0.26(2)
	137	0.48(3)
	138	0.71(9)
	139	0.99(6)
	140	1.15(6)
	141	1.34(7)
	142	1.37(5)
	143	1.28(9)
	144	1.12(7)
	145	1.02(4)

	146	0.92(5)
	147	0.77(4)
	148	0.63(4)
	149	0.56(2)
	150	0.58(3)
	151	0.48(3)
	152	0.39(2)
	153	0.22(3)
	154	0.11(3)
	155	0.023(6)
61	137	0.086(26)
	138	0.20(3)
	139	0.32(6)
	140	0.50(4)
	141	0.73(7)
	142	0.86(9)
	143	1.01(12)
	144	1.02(15)
	145	0.88(5)
	146	0.84(4)
	147	0.75(5)
	148	0.70(3)
	149	0.58(8)
	150	0.51(12)
	151	0.45(7)
	152	0.33(8)
	153	0.26(3)
	154	0.186(22)
	155	0.117(12)
	156	0.062(10)
62	142	0.33(6)
	143	0.47(8)
	144	0.65(10)
	145	0.70(7)
	146	0.75(7)
	147	0.700(28)
	148	0.645(45)
	149	0.572(40)
	150	0.51(8)
	151	0.436(22)
	152	0.35(3)
	153	0.267(11)
	154	0.203(16)
	155	0.15(2)
	156	0.10(2)
	157	0.054(15)
	158	0.029(7)

63	144	0.26(4)
	145	0.40(5)
	146	0.514(26)
	147	0.535(21)
	148	0.560(34)
	149	0.567(34)
	150	0.558(33)
	151	0.527(42)
	152	0.491(24)
	153	0.387(23)
	154	0.315(16)
	155	0.221(15)
	156	0.154(11)
	157	0.108(11)
	158	0.064(23)
	159	0.044(15)
	160	0.019(11)
64	147	0.26(4)
	148	0.34(4)
	149	0.429(34)
	150	0.454(45)
	151	0.47(12)
	152	0.476(24)
	153	0.45(5)
	154	0.34(5)
	155	0.29(3)
	156	0.24(3)
	157	0.17(2)
	158	0.12(2)
	159	0.077(14)
	160	0.052(7)
	161	0.028(5)
162	0.012(7)	

Table 5: Fission fragment isotopic cross sections measured in the present work. Statistical uncertainties are given on the last significant numbers, excluding the 10% systematical uncertainties.



- [1] G. Friedlander, L. Friedman, B. Gordon, and L. Yaffe, Phys. Rev. 129 (1963) 1809
- [2] R. Klapisch, Annual Review of Nuclear Sciences, Vol 19 (1969) 33  
and R. Klapisch, J. Chaumont, C. Philippe, I. Amarel, R. Ferreau, R. Salome  
and R. Bernas, Nucl. Inst. Methods 53 (1967) 216
- [3] B.N. Belyaev, V.D. Domkin, Yu.G. Korobulin, L. N. Androneko and G. E. Solyakin, Nucl. Phys. A348 (1980) 479
- [4] A. V. Prokofiev, Nucl. Inst. Methods A 463 (2001) 557
- [5] M. Gloris, R. Michel, F. Sudbrock, U. Herpers, P. Malmberg, B. Holmqvist, Nucl. Instrum. and Methods A 463 (2001) 593
- [6] Yu. E. Titarenko, O. V. Shvedov, M. M. Igumnov, S. G. Mashnik, E. I. Karpikhin, V. D. Kazaritsky, V. F. Batyaev, A. B. Koldobsky, V. M. Zhivun, A. N. Sosnin, R. E. Prael, M. B. Chadwick, T. A. Gabriel and M. Blann. Nucl. Instrum. and Methods A 414 (1998) 73
- [7] M. Bernas, C. Engelmann, P. Armbruster, S. Czajkowski, F. Ameil, C. Böckstiegel, Ph. Dessagne, C. Donzaud, H. Geissel, A. Heinz, Z. Janas, C. Kozhuharov, C. Miehé, G. Münzenberg, M. Pfützner, W. Schwab, C. Stéphan, K. Sümmerer, L. Tassan-Got and B. Voss, Phys. Lett B 415 (1997) 111
- [8] Ch. Engelmann, F. Ameil, P. Armbruster, M. Bernas, S. Czajkowski, Ph. Dessagne, C. Donzaud, H. Geissel, A. Heinz, Z. Janas, C. Kozhuharov, Ch. Miehé, G. Münzenberg, M. Pfützner, C. Röhl, W. Schwab, C. Stéphan, K. Sümmerer, L. Tassan-Got and B. Voss, Zeit. Phys. A352 (1995) 351
- [9] F. Carminati, R. Klapisch, J. P. Revol, Ch. Roche, J. A. Rubio, C. Rubbia. CERN Report CERN/AT/93-47(ET), 1993.
- [10] P. Armbruster, H. Geissel, G. Münzenberg, (GSI) Darmstadt, M. Bernas, (IPN) Orsay  
Patentschrift Deutsches Patentamt P 44 10 587.8.33, GSI Darmstadt 27.03.1994  
Brevet de l' Institut national de la propriété industrielle, Paris, France 95 03 499, GSI Darmstadt 24.03.1995
- [11] B. Mustapha, PhD Thesis Paris XI University (1999) IPNO-T-99-05
- [12] F. Rejmund, B. Mustapha, P. Armbruster, J. Benlliure, M. Bernas, A. Boudard, J. P. Dufour, T. Enqvist, R. Legrain, S. Leray, K.-H. Schmidt, C. Stéphan, J. Taieb, L. Tassan-Got and C. Volant, Nucl. Phys. A683 (2001) 481
- [13] J. Benlliure, P. Armbruster, M. Bernas, A. Boudard, J.-P. Dufour, T. Enqvist, R. Legrain, S. Leray, B. Mustapha, F. Rejmund, K.-H. Schmidt, C. Stéphan, L. Tassan-Got and C. Volant, Nucl. Phys. A683 (2001) 513

- [14] W. Wlazlo, T. Enqvist, P. Armbruster, J. Benlliure, M. Bernas, A. Boudard, S. Czajkowski, R. Legrain, S. Leray, B. Mustapha, M. Pravikoff, F. Rejmund, K.-H. Schmidt, C. Stéphan, J. Taieb, L. Tassan-Got and C. Volant, Phys. Rev. Lett. 84 (25) (2000) 5736
- [15] T. Enqvist, W. Wlazlo, P. Armbruster, J. Benlliure, M. Bernas, A. Boudard, S. Czajkowski, R. Legrain, S. Leray, B. Mustapha, M. Pravikoff, F. Rejmund, K.-H. Schmidt, C. Stéphan, J. Taieb, L. Tassan-Got and C. Volant, Nucl. Phys. A686 (2001) 481
- [16] T. Enqvist, P. Armbruster, J. Benlliure, M. Bernas, A. Boudard, S. Czajkowski, R. Legrain, S. Leray, B. Mustapha, M. Pravikoff, F. Rejmund, K.-H. Schmidt, C. Stéphan, J. Taieb, L. Tassan-Got, F. Vivès, C. Volant and W. Wlazlo, Nucl. Phys. A 703 (2002) 435
- [17] J. Taieb, PhD Thesis Paris XI University (2000) IPNO-T-00-10 and J. Taieb, P. Armbruster, J. Benlliure, M. Bernas, A. Boudard, E. Casajeros, S. Czajkowski, T. Enqvist, R. Legrain, S. Leray, B. Mustapha, M. Pravikoff, F. Rejmund, K.-H. Schmidt, C. Stéphan, L. Tassan-Got, C. Volant and W. Wlazlo, submitted to Nucl. Phys. A
- [18] E. Casarejos Ruiz, PhD Thesis, University de Santiago de Compostela (2001), GSI Rep. Diss.2002-04
- [19] P. Armbruster, M. Bernas, S. Czajkowski, H. Geissel, T. Aumann, Ph. Dessagne, C. Donzaud, E. Hanelt, A. Heinz, M. Hesse, C. Kozhuharov, Ch. Miehé, G. Münzenberg, M. Pfützner, K.-H. Schmidt, W. Schwab, C. Stéphan, K. Sümmerer, L. Tassan-Got and B. Voss, Z. Phys. A355 (1996) 191
- [20] C. Donzaud, S. Czajkowski, P. Armbruster, M. Bernas, C. Böckstiegel, Ph. Dessagne, H. Geissel, E. Hanelt, A. Heinz, C. Kozhuharov, Ch. Miehé, G. Münzenberg, M. Pfützner, W. Schwab, C. Stéphan, K. Sümmerer, L. Tassan-Got, B. Voss, Eur. Phys. J. A1, 407-426 (1998)
- [21] W. Schwab, M. Bernas, P. Armbruster, S. Czajkowski, Ph. Dessagne, C. Donzaud, H. Geissel, A. Heinz, C. Kozhuharov, C. Miehé, G. Münzenberg, M. Pfützner, C. Stéphan, K. Sümmerer, L. Tassan-Got and B. Voss, Eur. Phys. J. A2 (1998) 179
- [22] T. Enqvist, J. Benlliure, F. Farget, K.-H. Schmidt, P. Armbruster, M. Bernas, L. Tassan-Got, A. Boudard, R. Legrain, C. Volant, C. Böckstiegel, M. de Jong and J.-P. Dufour, Nucl. Phys. A 658 (1999) 47
- [23] Ch. Engelmann, Thesis Universität Tübingen (1998), GSI Rep. Diss. 1998-15
- [24] R. E. Prael, H. Liechtenstein, Los Alamos-UR-89-3014, 1989
- [25] J.-J. Gaimard and K.-H. Schmidt, Nucl. Phys. A 531 (1991) 709.
- [26] A. R. Junghans, M. de Jong, H.-G. Clerc, A. V. Ignatyuk, G.A. Kudyaev, K.-H. Schmidt, Nucl. Phys. A 629 (1998) 635
- [27] J. Benlliure, A. Grewe, M. de Jong, K.-H. Schmidt and S. Zhdanov, Nucl. Phys. A 628 (1998) 458

- [28] A. Boudard, J. Cugnon, S. Leray and C. Volant, Phys. Rev. C 66 (2002) 044619
- [29] B. Jurado, K.-H. Schmidt and K.-H. Behr, Nucl. Inst. Methods A483 (2002) 603
- [30] P. Chesny, A. Forges, J.M. Gheller, G. Guiller, P. Pariset, L. Tassan-Got, P. Armbruster, H.-H. Behr, J. Benlliure, K. Burkard, A. Brünle, T. Enqvist, F. Farget, K.-H. Schmidt, GSI Annual Report 1996, GSI 1997-1 p. 190.
- [31] C. Scheidenberger, Th. Stöhlker, W. E. Meyerhof, H. Geissel, P. H. Mokler and B. Blank, Nucl. Inst. and Methods 142 (1998) 441
- [32] H. Geissel, P. Armbruster, K.-H. Behr, A. Brünle, K. Burkard, M. Chen, H. Folger, B. Franczak, H. Keller, O. Klepper, B. Langenbeck, F. Nickel, E. Pfeng, M. Pfützner, E. Roeckl, K. Rykaczewski, I. Schall, D. Schart, C. Scheidenberger, K.-H. Schmidt, A. Schröter, T. Schwab, K. Sümmerer, M. Weber, G. Münzenberg, T. Brohm, H.-G. Clerc, M. Fauerbach, J.-J. Gaimard, A. Grewe, E. Hanelt, B. Knödler, M. Steiner, B. Voss, J. Weckenmann, C. Ziegler, A. Magel, H. Wollnik, J.-P. Dufour, Y. Fujita, D. J. Vieira, B. Sherill, Nucl. Inst. and Methods B 70 (1992) 286
- [33] M. Pfützner, H. Geissel, G. Münzenberg, F. Nickel, C. Scheidenberger, K.-H. Schmidt, K. Sümmerer, T. Brohm, B. Voss and H. Bichsel, Nucl. Inst. and Methods B86 (1994) 213
- [34] B. Voss, T. Brohm, H.-G. Clerc, A. Grewe, E. Hanelt, A. Heinz, M. de Jong, A. Junghans, W. Morawek, C. Röhl, S. Steinhäuser, C. Ziegler, K.-H. Schmidt, K.-H. Behr, H. Geissel, F. Nickel, C. Scheidenberger, K. Sümmerer and A. Magel, Nucl. Inst. and Methods A 364 (1995) 150
- [35] B.A. Bochagov, V.S. Bychenkov, V.D. Dmitriev, S.P. Mal'tsev, A.I. Obukhov, N.A. Perfilov and O. E. Shigaev, Sov. J. Nucl. Phys. 28 (2) (1978) 291
- [36] J. Benlliure, J. Pereira-Conca and K.-H. Schmidt, Nucl. Instrum. and Methods A478 (2002) 493
- [37] Th. Schwab, GSI report 91-10 (1991)
- [38] B.D. Wilkins, E.P. Steinberg, R.R. Chasman, Phys. Rev. C14 (1976) 1832
- [39] C. Böckstiegel, S. Steinhäuser, J. Benlliure, H.-G. Clerc, A. Grewe, A. Heinz, M. de Jong, A.R. Junghans, J. Müller, K.-H. Schmidt, Phys. Lett. B 398 (1997) 259
- [40] J. Pereira-Conca, PhD Thesis, in progress, Univ. Santiago de Compostela, private communication.
- [41] P. Napolitani, P. Armbruster, M. Bernas and L. Tassan-Got, to be submitted to Nucl. Phys. A
- [42] P.J. Karol, Phys. Rev. C 11 (1975) 1203
- [43] J. Chaumont, PhD Thesis Univ. of Paris XI (1970)  
[csnwww.in2p3.fr/AMDC/experimental/th-chaumont.pdf](http://csnwww.in2p3.fr/AMDC/experimental/th-chaumont.pdf)

- [44] M. V. Ricciardi, K.-H. Schmidt, J. Benmure, I. Enqvist, F. Allen, F. Armbruster, M. Bernas, A. Boudard, S. Czajkowski, R. Legrain, S. Leray, B. Mustapha, M. Pravikoff, C. Stephan, L. Tassan-Got, C. Volant, proceedings of the XXXIX Int. Winter Meeting on Nucl. Phys., Bormio, Italy (2001).  
M. V. Ricciardi, PhD Thesis in progress, GSI-Darmstadt.
- [45] L.A. Vaishnane, L.N. Andronenko, G.G. Kovshevny, A.A. Kotov, G.E. Solyakin and W. Neubert, *Z. Phys. A* 302 (1981) 143
- [46] B. Jurado, PhD Thesis, Compostela (2002), Diss. GSI Rep. 2002-10
- [47] T. Brohm, PhD thesis, TU-Darmstadt, (1994)
- [48] P. Armbruster, *Nucl. Phys. A*140, (1970) 385
- [49] K. Sistemich, P. Armbruster, J. Eidens and E. Roeckl, *Nucl. Phys. A*139 (1969) 289
- [50] H. U. Wenger, F. Botta, R. Chawla, M. Daum, D. Gavillet, Z. Kopajtic, D. Ledergerber, H. P. Linder and S. Röllin, *Annals of Nucl. Energy* 26 (1999) 141
- [51] R. Silberberg, C. H. Tsao, A. F. Barghouty, *Astrophys. J.* 501 (1998) 911 and (Tsao@nrl.navy.mil) *Phys. Report* 191, 351 (1990)
- [52] L. Dresner, ORNL-TM-7882, Oak Ridge National Laboratory, 1981.
- [53] S.I. Mulgin, K.-H. Schmidt, A. Grewe, S. V. Zhdanov, *Nucl. Phys. A* 640 (1998) 375.
- [54] U. Brosa, S. Grossmann, A. Müller, *Phys. Rep.* 197 (1990) 167
- [55] A.V. Ignatyuk, G. N. Smirenkin and A. S. Tishin, *Sov. J. Nucl. Phys.* 21 (1975) 255.
- [56] D. Hilscher, U. Jahnke, F. Goldenbaum, L. Pienkowski, J. Galin and B. Lott, *Nucl. Inst. and Methods A*414 (1998) 100